

1 **Modulation of the seasonal cycle of the Antarctic sea ice extent by sea ice**
2 **processes and feedbacks with the ocean and the atmosphere**

3

4 Hugues Goosse¹, Sofia Allende Contador¹, Cecilia M. Bitz², Edward Blanchard-Wrigglesworth², Clare
5 Eayrs³, Thierry Fichefet¹, Kenza Himmich⁴, Pierre-Vincent Huot⁵, François Klein¹, Sylvain Marchi⁵,
6 François Massonnet¹, Bianca Mezzina¹, Charles Pelletier⁶, Lettie Roach^{7,8}, Martin Vancoppenolle⁴,
7 Nicole P.M. van Lipzig⁵

- 8 1. Earth and Life Institute, Université catholique de Louvain, Belgium
9 2. Department of Atmospheric Sciences, University of Washington, Seattle, USA
10 3. ~~Korea Polar Research Institute, Incheon, South Korea. Center for global Sea Level Change,~~
11 ~~New York University Abu Dhabi, United Arab Emirates~~
12 4. Sorbonne Université, Laboratoire d'Océanographie et du Climat (LOCEAN-IPSL), CNRS, IRD,
13 MNHN, Paris, France
14 5. Department of Earth and Environmental Sciences, KU Leuven, Leuven, Belgium
15 6. European Centre for Medium-Range Weather Forecasts, Bonn, Germany
16 7. NASA Goddard Institute for Space Studies, New York, NY, USA
17 8. Center for Climate Systems Research, Columbia University, New York, NY, USA

Mis en forme : Anglais (États-Unis)

18
19

20
21 Corresponding author: Hugues Goosse hugues.goose@uclouvain.be

Code de champ modifié

22

23 Revised version 1. 05-01-23

24

25 **Abstract**

26 The seasonal cycle of the Antarctic sea ice extent is strongly asymmetric, with a relatively slow increase
27 after the summer minimum followed by a more rapid decrease after the winter maximum. This cycle
28 is intimately linked to the seasonal cycle of the insolation received at the top of the atmosphere but
29 sea ice processes as well as the exchanges with the atmosphere and ocean may also play a role. To
30 quantify these contributions, a series of idealized sensitivity experiments have been performed with
31 an eddy-permitting (1/4°) NEMO-LIM3 Southern Ocean configuration, including a representation of ice
32 shelf cavities, in which the model was either driven by an atmospheric reanalysis or coupled to the
33 COSMO-CLM² regional atmospheric model. In those experiments, sea ice thermodynamics and
34 dynamics as well as the exchanges with the ocean and atmosphere are strongly perturbed. This
35 perturbation is achieved by modifying snow and ice thermal conductivities, the vertical mixing in the
36 ocean top layers, the effect of freshwater uptake/release upon sea ice growth/melt, ice dynamics and
37 surface albedo. We find that the evolution of sea ice extent during the ice advance season is largely
38 independent of the direct effect of the perturbation and appears thus mainly controlled by initial state
39 in summer and subsequent insolation changes. In contrast, the melting rate varies strongly between
40 the experiments during the retreat, in particular if the surface albedo or sea ice transport are modified,
41 demonstrating a strong contribution of those elements to the evolution of ice coverage through spring
42 and summer. As with the advance phase, the retreat is also influenced by conditions at the beginning
43 of the melt season in September. Atmospheric feedbacks enhance the model winter ice extent
44 response to any of the perturbed processes, and the enhancement is strongest when the albedo is
45 modified. The response of sea ice volume and extent to changes in entrainment of subsurface warm
46 waters to the ocean surface is also greatly amplified by the coupling with the atmosphere.

47 **Short Summary** (500 characters)

48 Using idealized sensitivity experiments with a regional atmosphere-ocean-sea ice model, we show that
49 the sea ice advance is constrained by initial conditions in March while the retreat season is influenced
50 by the magnitude of several physical processes, in particular by the ice-albedo feedback and ice
51 transport. Atmospheric feedbacks amplify the response of the winter ice extent to perturbations while
52 some negative feedbacks related to heat conduction fluxes act on the ice volume.

53

54 **1. Introduction**

55 The sea ice extent in the Southern Ocean, defined as the ocean surface covered by at least 15% of
56 sea ice, displays a very pronounced seasonal cycle with a minimum in February of about 3 million km²
57 and a maximum in September of more than 18 million km² on average over the last decades (Parkinson,
58 2014, 2019; Handcock and Raphael, 2020) (Fig. 1). In contrast to the Arctic, where multiyear ice
59 accounted for a significant fraction of the total ice extent --at least until the end of the 20th century--
60 , the Antarctic sea ice cover is mainly seasonal, with sea ice only present in summer in some regions
61 close to the coast, in particular in the Weddell and Ross Seas.

62 The seasonal cycle of Antarctic sea ice extent is highly asymmetric, with a minimum around Julian
63 day 50 (February 19) and a maximum on average close to day 260 (September 18) (Stammerjohn et
64 al., 2008; Massom et al., 2013; Handcock and Raphael, 2020; Raphael et al., 2020; Roach et al., 2022).
65 The advance season, defined as the time between the minimum and maximum ice extents, is thus
66 about two months longer than the retreat season, defined as the time from maximum to minimum.

67 It has been suggested that this asymmetry is related to the variations of the mean position of the
68 westerly winds that blow over the Southern Ocean associated with the Semi Annual Oscillation (SAO)
69 (Enomoto and Ohmura, 1990; Watkins and Simmonds, 1999; Eayrs et al., 2019). This mode of variability
70 of the Antarctic climate induces a larger divergence of the sea ice pack in spring and thus a rapid
71 melting, while the divergence is weaker in autumn, leading to a slower expansion of the pack. A
72 complementary mechanism explaining the rapid seasonal retreat of the sea ice is the positive ice-
73 albedo feedback, in which a decrease in ice concentration yields a larger absorption of solar radiation
74 and enhances the ice melting (Gordon, 1981; Nihashi and Cavalieri, 2006). A possible role of the
75 oceanic heat input has also been proposed (Gordon, 1981). However, the vertical ocean heat transport
76 from the relatively warm ocean below the mixed layer to the surface is higher in autumn and winter
77 when the stratification is weak than in spring and summer when it is strong (Gordon, 1981; Martinson,
78 1990). The seasonality of the vertical oceanic transport alone could thus not explain the asymmetry in
79 the seasonal cycle of the sea ice extent (Eayrs et al., 2019), but it could have an indirect effect, for
80 instance through its effect on the ice thickness (Martinson, 1990; Goosse et al., 2018; Wilson et al.,
81 2019).

82 Nevertheless, a recent study based on idealized climate models has demonstrated that the
83 asymmetry of the seasonal cycle of the ice extent is due to the seasonal cycle of incoming solar
84 radiation (Roach et al., 2022). The period with relatively high incoming solar radiation in spring and
85 summer induces a rapid melting season and a fast retreat of the sea ice, while a long period with low
86 insolation in autumn and winter favors a longer growing season. This relatively direct mechanism is
87 very robust and explains why the asymmetry is observed each year and is reproduced by a wide range
88 of models, from very simple ones to the most complex Earth System ~~models~~-Models (Eayrs et al., 2019;
89 Roach et al., 2022).

90 Identifying the seasonal cycle of insolation as the main contributor to the asymmetry of the
91 seasonal cycle of the Antarctic sea ice extent is a major achievement. However, the atmosphere, sea
92 ice and ocean dynamics still play a role and may modulate the magnitude of the asymmetry.
93 Furthermore, the seasonal cycle of the sea ice extent is characterized by many other elements in
94 addition to this asymmetry, such as its amplitude or the timing of the maximum retreat. Factors
95 controlling those characteristics also need to be analyzed to quantify how the seasonal cycle of the
96 Antarctic sea ice influences the dynamics of the climate at high southern latitudes. Models still have
97 large biases on those aspects and a better understanding is necessary for model improvement (Downes
98 et al., 2015; Eayrs et al., 2019; Roach et al., 2020; Raphael et al., 2020; Schroeter and Sandery, 2022).

99 Several studies have addressed the role of sea ice processes and atmosphere and ocean feedbacks
100 on Antarctic sea ice extent, focusing both on the mean seasonal cycle and the interannual variability
101 (e.g., Fichefet and Morales Maqueda, 1997; Holland and Kimura, 2016; Hobbs et al., 2016; Kushara et
102 al., 2019). An instructive diagnostic is to decompose the contribution of the dynamics, including the
103 transport of sea ice, from the one of thermodynamics that influences the local formation or melting of
104 sea ice. This decomposition is not always straightforward, as for example winds control both the sea
105 ice transport and the advection of warm or cold air masses that impacts thermodynamic processes.
106 The results may also depend on the definition of the dynamics and thermodynamics contributions.
107 Nevertheless, a common conclusion is that the thermodynamic processes play a strong role nearly all
108 year long, with a clearly dominant contribution during the advance period, while the impact of the
109 winds becomes more important later in the season, in particular during the retreat (Fichefet and
110 Morales Maqueda, 1997; Holland and Kimura, 2016; Kushara et al., 2019; Eays et al., 2020).

111 Despite those advances, many uncertainties remain around the processes controlling the seasonal
112 cycle of the Antarctic sea ice, in particular because the majority of existing studies address only some
113 of the processes, forbidding a comparison between different factors, or are devoted to the variability
114 and trends, not to the seasonal cycle itself. As a consequence, our goal here is to propose an analysis
115 of the different processes in a single framework, using sensitivity experiments designed to the study
116 of the seasonal cycle. Specifically, we perform sensitivity experiments with a sea-ice-ocean model
117 driven by an atmospheric reanalysis and the same model coupled to a regional atmospheric model,
118 disabling or strongly perturbing key processes related to sea ice dynamics and thermodynamics as well
119 as the exchanges between the atmosphere and ocean.

120 The goal of those sensitivity experiments is not to impose realistic changes or to improve
121 agreement with observations but rather to determine the role of the associated processes. In contrast
122 to many existing sensitivity studies performed with sea ice-ocean models, the experiments with the
123 coupled model will address the limitations associated with a prescribed atmospheric state, which tends
124 to damp the changes imposed by the perturbation as the location of the sea ice edge is strongly
125 controlled by the atmospheric forcing, in particular in winter (e.g., Urrego-Blanco et al, 2016).
126 Furthermore, the comparison between the experiments with and without coupling with the
127 atmosphere will, for the first time, quantify the regional atmospheric feedbacks in response to the
128 imposed perturbation. The sensitivity experiments last only two years and are not analyzed at
129 equilibrium for two reasons. First, the drift of the model state after several years in response to the
130 perturbation can be large. The relative importance of the various processes, which may depend of the
131 mean state, can thus be very different from the one in the current climate. Second, by comparing the
132 first years of each experiment, which start with identical conditions at the beginning of the season,
133 and the second year, for which the perturbation has already acted during one year, we can determine
134 the contribution of the initial state and the one of the processes occurring during the sea ice advance
135 and retreat seasons. This approach is also instructive for understanding observed changes and for
136 predictions as this distinction between initial conditions and ongoing perturbations is key in
137 interpreting the observed variability. Many studies have demonstrated that large spatial variations are
138 present between the different sectors of the Southern Ocean (e.g., Parkinson et al., 2019; Kushara et
139 al., 2019; Kacimi and Kwok, 2020). Analyzing them is necessary to have a full picture of the dynamics
140 of the system. Nevertheless, we will focus here first on the ice extent integrated over the whole
141 Southern Ocean, keeping the regional changes for future work except when critically needed to
142 interpret the integrated changes. The models used and the perturbation applied are described in
143 Section 2. Section 3 presents the main results of the sensitivity experiments. Section 4 is devoted to
144 the atmospheric feedbacks. Section 5 includes a discussion and a synthesis of our main results.

145

146 **2 Methodology**

147 Model description

148 The simulations are performed with a regional circum-Antarctic configuration of the sea-ice-ocean
149 model NEMO-LIM3 version 3.6 (Rousset et al., 2015) driven by the ERA5 atmospheric reanalysis
150 (Hersbach et al., 2020) and with NEMO-LIM3 coupled to the COSMO-CLM² regional atmospheric model
151 (Pelletier et al., 2022a). The model set-up and forcing are identical to Verfaillie et al. (2022) for NEMO-
152 LIM3 driven by ERA5 and to Pelletier et al. (2022a) for NEMO-LIM-COSMO-CLM², except that, for the
153 latter, a bug in the interpolation of the winds in the coupling between the ocean and atmosphere has
154 been corrected (Pelletier et al., 2022b). The version of NEMO-LIM3 driven by ERA5 will hereafter be
155 referred to as NEMO and the version coupled to COSMO-CLM² as PARASO following Pelletier et al.
156 (2022a).

157 NEMO (Nucleus for European Modelling of the Ocean, Madec et al., 2017) includes the OPA ocean
158 model (Océan PARallélisé) coupled with the Louvain-la-Neuve sea ice model (Vancoppenolle et al.,
159 2012; Rousset et al., 2015). Our configuration has an explicit representation of Antarctic ice shelf
160 cavities using the implementation of Mathiot et al. (2017). The free-surface oceanic component is
161 hydrostatic and applies finite differences to solve the equations on an Arakawa C-grid. Vertical mixing
162 is computed using a turbulent kinetic energy (TKE) scheme (Gaspar et al., 1990), while lateral diffusion
163 of momentum is carried out with a bi-Laplacian viscosity and isopycnal diffusion of tracers with a
164 Laplacian operator. Oceanic convection is represented using an enhanced vertical diffusivity, triggered
165 under unstable vertical stratification (Lazar et al., 1999). The sea ice component uses an elastic-viscous-
166 plastic rheology (Bouillon et al., 2013) and a five-category ice-thickness distribution (Bitz et al., 2001;
167 Massonnet et al., 2019). Each of those categories is covered by snow, with one snow thickness per
168 category. The energy conserving sea ice thermodynamics follows Bitz and Lipscomb (1999) and
169 includes an explicit representation of the evolution of salt content and its impact on the sea ice
170 properties (Vancoppenolle et al., 2009). The albedo of sea ice depends on snow and ice thickness,
171 surface temperature and cloud cover (Grenfell and Perovich, 2004; Brandt et al., 2005).

172 The model grid is ePERIANT025 (Mathiot et al., 2017) that has a nominal horizontal resolution of $\frac{1}{4}$
173 of a degree with an isotropic spacing, meaning that the resolution is about 24 km at 30°S but increases
174 up to 3.8 km over the Antarctic continental shelf. A z-coordinate is applied on the vertical using 75
175 levels, with a thickness of about 1m at surface reaching 200m at depth and partial steps in the bottom
176 layer (and in the top layer beneath ice shelves). In the uncoupled simulations, NEMO is driven at the
177 surface by the fluxes computed by the CORE bulk formulas (Large et al., 2004) using 3-hourly fields
178 derived from the ERA5 reanalysis (Hersbach et al., 2020). The conditions at the northern boundary of
179 the domain (30°S) are prescribed from the ORAS5 ocean reanalysis (Zuo et al., 2019).

180 In PARASO, NEMO is coupled to COSMO-CLM², which includes the version 5.0 of the Consortium
181 for Small-scale MOdeling (COSMO) regional atmospheric model (Rockel et al., 2008) and the
182 Community Land Model version 4.5 (Oleson et al., 2013). COSMO is a non-hydrostatic model using
183 generalized terrain-following height coordinates with 60 levels (Doms and Baldauf, 2018). The version
184 utilized here includes parameter calibration adapted to polar regions and a new snow scheme
185 (Souverijns et al., 2018). Furthermore, the computation of the fluxes is separated over land, ocean and
186 sea ice surfaces for the coupling with NEMO (Pelletier et al., 2022a). The conditions at the lateral
187 boundary of the domain are obtained from ERA5. COSMO-CLM² uses a rotated latitude-longitude grid
188 with a horizontal resolution of 0.22°, which corresponds to about 25 km. The domain is smaller than

189 the one of NEMO, with a northern boundary located between 50°S and 40°S. In the areas not simulated
190 by COSMO-CLM², NEMO is forced by ERA5 fields as in the uncoupled configuration.

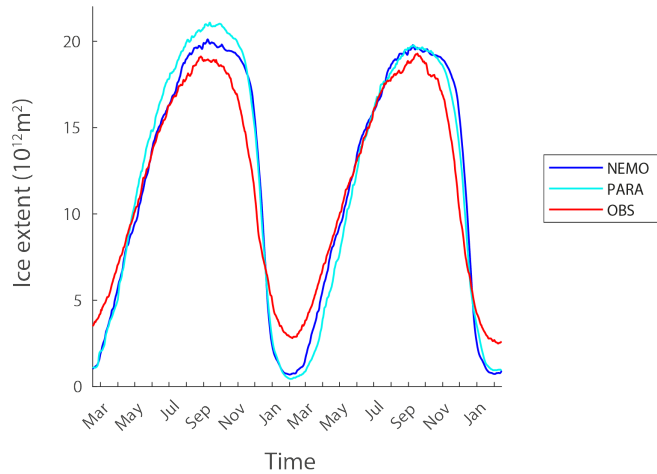
191 Experimental design

192 NEMO is driven by the ERA5 reanalysis using every year the forcing from the period 1st May 1990
193 to 30th April 1991, which is considered a normal period regarding the major modes of climate
194 variability (Stewart et al., 2020; Verfaillie et al., 2022). ~~This simulation~~The forcing thus has no
195 interannual variability in order to focus specifically on the seasonal cycle, while keeping conditions
196 close to the model climatology. The two-year simulations analyzed here follow a 10-year spin-up,
197 which is sufficient to have a quasi-equilibrium for the surface variables (Verfaillie et al., 2022). The
198 PARASO simulation has been initialized in 1985 and we discuss here two-year simulations following a
199 10-year spinup, meaning that the analyses start in 1995. The conditions are thus slightly different in
200 the two configurations. Nevertheless, the mean states of the coupled and uncoupled models are also
201 different, forbidding a direct comparison between them anyway (Fig. 1). Both configurations
202 underestimate the sea ice extent in summer, and tend to overestimate it in winter. They also have a
203 delayed and too rapid retreat season. Those biases are similar to those found in many other coupled
204 and uncoupled models (Downes et al., 2015; Eayrs et al., 2019; Roach et al., 2020; Raphael et al., 2020;
205 Schroeter and Sandery, 2022). Each sensitivity experiment will be compared to the reference
206 simulation using the same model configuration and initial state. ~~This standard method implicitly~~
207 ~~assumes that the biases remain nearly constant in those pairs of experiments and the effect of those~~
208 ~~biases assuming that the biases are small enough to have only a marginal effect on the quantification~~
209 ~~of the response to the perturbation is largely removed by performing the difference between the~~
210 ~~experiment results. However, even with this procedure, the biases can still have in some cases a clear~~
211 ~~impact on the quantification of feedbacks, as discussed in section 4 for the summer sea ice extent.~~
212 ~~Additionally, in NEMO alone, the model internal variability is very low for the surface variables analyzed~~
213 ~~in the present study because of the strong constraint provided by the atmospheric forcing. Due to the~~
214 ~~inclusion of an interactive atmosphere, PARASO can develop some internal variability within its domain~~
215 ~~despite the fixed condition imposed at the boundaries. Additionally, in contrast to NEMO alone,~~
216 ~~PARASO can develop some internal variability despite the strong constraints at its boundaries.~~Ideally,
217 an ensemble of simulations should be performed for each of the coupled experiments, but this exceeds
218 available computing capacities. Tests with identical configurations but slight perturbations of the initial
219 state indicate that the difference in ice extent due to this internal variability of the model is usually
220 much smaller than 0.2 million km², i.e. less than the response to the perturbation in the majority of
221 the experiments, but the possibility that some of the differences between the experiments are just
222 occurring by chance must be kept in mind.

Mis en forme : Couleur de police : Automatique

Mis en forme : Couleur de police : Automatique

Mis en forme : Couleur de police : Automatique



223
 224 Figure 1. Seasonal cycle of the Antarctic sea ice extent (in 10^{12} m²) in observations (Fetterer et al.,
 225 2017) and in the reference experiments with NEMO and PARASO (starting in March). For observations
 226 and PARASO, the period from March 1995 to February 1997 is shown while for NEMO the forcing
 227 corresponds to the ‘normal period’ from May 1990 to April 1991 that is applied twice.

228 Set-up of the sensitivity experiments

229 Identical perturbations are applied in NEMO and PARASO on the 1st of March and 1st of September
 230 in the 2-year sensitivity experiments (see Table 1). The first two experiments are devoted to the role
 231 of the exchanges between sea ice and the oceanic mixed layer. In the first one (Mix100), the ocean
 232 temperatures and salinities are homogenized from the surface to 100m depth at each time step by
 233 completely mixing the corresponding grid boxes in each column. This depth roughly corresponds to
 234 the seasonal maximum depth of the mixed layer in the model in most ice-covered regions except over
 235 the continental shelf (e.g., Barthélemy et al., 2015). The effect of this mixing scheme perturbation is
 236 that the seasonal summer shoaling of the mixed layer due to freshening is removed. The goal is to
 237 determine whether such deep summer mixing favors heat storage at the surface and delays the sea
 238 ice advance. In the second experiment (NoMassFlux), sea ice growth and melt is no longer associated
 239 with freshwater uptake and release. In practice, we thus set all the mass fluxes at the sea ice-ocean
 240 interface to zero in NoMassFlux but this is equivalent to assuming that sea ice salinity is the same as
 241 the ocean surface salinity. Therefore, the surface ocean salinity no longer responds to sea ice formation
 242 and melting. This modification disables the negative ice production-entrainment feedback (Martinson,
 243 1990) in which the upper ocean salinity increase due to ice formation induces a mixed layer deepening
 244 and entrainment of deeper warmer water towards the surface that reduces ice formation. The absence
 245 of this negative feedback in NoMassFlux could thus potentially accelerate the sea ice advance.

246 The second group of experiments is devoted to sea ice physics and properties. As sea ice thickness
 247 is a key characteristic of the pack that strongly controls its behavior, the first two experiments
 248 artificially increase (ThickIce) and decrease (ThinIce) the ice thickness. This is achieved by increasing
 249 the thermal conductivities of the ice and snow by a factor of five in ThickIce and by decreasing the
 250 thermal conductivities of the ice and snow by a factor of five in ThinIce. This is achieved by increasing
 251 (ThickIce) and decreasing (ThinIce) the thermal conductivities of the ice and snow by a factor of five.
 252 With low conductivity, ice becomes a much better insulator for the ocean that loses less heat to the

Mis en forme : Couleur de police : Automatique

253 atmosphere in fall and winter, inducing a slower increase in ice thickness (Maykut, 1986; Bitz and Roe,
 254 2004). From the results of ThickIce and ThinIce, we expect-intend to test the hypothesis then that a
 255 thinner ice will melt faster in spring, accelerating the ice retreat. As the ice-albedo feedback is expected
 256 to be a dominant element of the seasonal sea ice retreat (Gordon, 1981; Nihashi and Cavalieri, 2006),
 257 setting both the albedo of the snow and ice to the ocean value in AlbOce should accelerate the retreat.

258 We also test-quantify the impact of ice dynamics by disabling it (NoIcDyn). The ice dynamics are
 259 expected to favor a faster sea ice advance in fall by transporting sea ice from the colder regions, where
 260 it is quickly replaced because of strong ice formation, to the north where it can survive because of the
 261 relatively low temperature. It also accelerates the retreat in spring by transferring sea ice to regions
 262 where it is warm enough during this season to quickly melt and by creating leads within the pack that
 263 enhances the ice-albedo feedback (Fichefet and Morales Maqueda, 1997; Holland and Kimura, 2016;
 264 Kushahara et al., 2019; Eayrs et al., 2020). Suppressing ice dynamics should thus reduce the amplitude
 265 of the seasonal cycle of the sea ice extent (e.g., Fichefet and Morales Maqueda, 1997). For technical
 266 reasons, the implementation of sea-ice dynamics suppression differs in uncoupled and coupled
 267 experiments: in the former, all the sea-ice dynamic components of the model are disabled; in the latter,
 268 solely the velocity and large-scale transport is set to zero in PARASO (other mechanisms such as ridging
 269 are active).

270 Although no sensitivity experiment includes explicit modifications of atmospheric parameters or
 271 processes, all of the applied perturbations affect indirectly the exchanges between the ocean-sea-ice
 272 system and the atmosphere by modifying the surface conditions. Comparing the coupled and
 273 uncoupled configurations quantifies then the contribution of the atmospheric feedbacks. While the
 274 perturbations can potentially influence the atmospheric dynamics, and thus winds for instance, we will
 275 focus on the feedbacks related to heat exchanges at the surface as they are more directly impacted in
 276 the sensitivity experiments.

277
 278 Table 1. List of experiments. Each experiment is performed for 2 years with NEMO and PARASO
 279 and for two starting dates, March 1 and September 1. For references in the text, NEMO and PARASO
 280 experiments have the additional suffixes NEMO and PARA, respectively, while for the two starting
 281 dates we use the suffixes Mar and Sep.

Short name	Description
Ref	Reference experiment without perturbation
Mix100	Ocean mixed over the top 100m of the ocean all year long
NoMassFlux	No mass flux associated with the sea ice formation or melting
ThickIce	Sea ice and snow thermal conductivities multiplied/divided by 5
ThinIce	Sea ice and snow thermal conductivities divided/multiplied by 5
AlbOce	Sea ice and snow albedos equal to that of the ocean (=0.088)
NoIcDyn	Ice dynamics disabled (uncoupled mode); or sea ice velocity equals zero (coupled mode).

282

283 3 Results

284 *First advance season*

285 In the sensitivity experiments starting in March, the perturbations applied to the model physics
 286 have very little impact on the sea ice advance until August (Fig. 2ab and Fig. S1), both in the coupled
 287 and uncoupled model configurations. When starting from identical initial conditions, the sea ice

Mis en forme : Anglais (États-Unis)

Mis en forme : Couleur de police : Automatique

Mis en forme : Couleur de police : Automatique

288 advance seems thus controlled by external conditions imposed by the seasonal evolution of the
289 insolation and does not depend much on the sea ice physics or on the interactions between sea ice,
290 the ocean and the atmosphere. Even the absence of sea ice transport (experiment
291 NolceDyn_NEMO_Mar and NolceDyn_PARA_Mar) has nearly-noa weak effect on the total sea ice
292 extent during this period, confirming previous studies indicating that the sea advance is mainly of
293 thermodynamic nature (e.g., Fichefet and Morales Maqueda, 1997; Kusahara et al., 2019). The impact
294 on the sea ice volume is more immediate, with a difference that can reach more than a factor two in
295 August between some experiments such as ThickIce_NEMO_Mar and Thin_NEMO_Mar (Fig. 3a).
296 Nevertheless, this change in volume has little impact on the extent, showing a decoupling between the
297 two variables in our experiments during this first advance season.

298 The different experiments have varying ice growth rates, consistent with the differences in ice
299 volume, but the temporal evolution is relatively similar during the advance season (Fig. 4 and Fig. S2).
300 ThickIce and NoMassflux stand as exceptions. In ThickIce, the ice production-entrainment feedback is
301 very active as a consequence of the large sea ice formation and brine release that destabilizes the
302 water column. The oceanic mixed layer depth (Fig. S4S3) is thus much larger than in the other
303 experiments and the associated vertical ocean-to-ice sensible heat transfer compensates early in the
304 season for a significant fraction of the cooling imposed at surface, explaining the early peak in the
305 freezing rate (for instance the peak occurs in day 166 in ThickIce_NEMO_Mar compared to day 220 in
306 the corresponding reference simulation). In NoMassFlux, by contrast, as the ice production-
307 entrainment feedback is inactive by design, the oceanic mixing is much weaker and strong ice
308 formation can be sustained until the end of the growth season, particularly in the PARASO
309 configuration, with a peak in ice formation in NoMassFlux_PARA_Mar on day 247 compared to day
310 187 in the corresponding reference simulation.

311 *Maximum extent and retreat season*

312 The modification of the ice volume imposed by the perturbations has only a weak impact on the
313 sea ice extent until August, as indicated above. However, but the experiments with thicker ice tend
314 to have a larger sea ice extent after August, a longer plateau with an extent close to the maximum,
315 and a slower retreat. For instance This impact of the ice thickness is well illustrated by, the comparison
316 between ThickIce_NEMO_Mar and Thin_NEMO_Mar, which have a difference of ice volume in winter
317 of more than $20 \cdot 10^{12} \text{ m}^3$. ThickIce_NEMO_Mar, which has the largest volume for all the experiments
318 with NEMO, has a maximum ice extent that is higher than in Thin_NEMO_Mar by 1.2 million km^2 , a
319 delayed beginning of the retreat timing of the maximum extent delayed by 42 days in this
320 experiment compared to Thin_NEMO_Mar, and an extent that is larger than in Thin_NEMO_Mar by 3.3
321 million km^2 at the end of November (Fig. 2a and Fig. S1). The impact of volume differences on the date
322 of the maximum extent itself is generally weak for most of the other experiments (see Tables 2 and 3),
323 but a link between the maximum volume and the date at which the sea ice extent decreases to 95% of
324 its maximum is clear in most experiments of them (Fig. 5a).

325 Thicker ice in September tends thus to delay sea ice retreat, as expected. However, the conditions
326 in September (which integrate the effect of the perturbation in model physics since March in the
327 simulations started at that time) are not the only reason for the difference between the experiments
328 during the retreat season. The experiments starting in September from identical initial conditions tend
329 to diverge nearly immediately, indicating a larger control of sea ice physics on the evolution of the ice
330 extent at this time of the year compared to the advance season (Fig. 2cd).

331 This large role for sea ice physics in the melt season is illustrated by the larger differences between
332 the experiments for the timing of maximum of the ice melting than for the timing of maximum ice

Mis en forme : Exposant

Mis en forme : Exposant

333 growth rate (Fig. 4 and Fig. S2). The maximum ice melting rate spans a range of up to 50 days between
334 the experiments that have the earliest melting (AlbOce) and the latest one (ThickIce, NoMassFlux and
335 No_Ice_Dyn). The faster and earlier melting occurs in experiments AlbOce, as the low albedo in those
336 experiments allows a stronger absorption of incoming solar radiation and thus a larger amount of melt
337 as soon as the Sun is high enough above the horizon. In AlbOce experiments, a large part of the retreat
338 is already achieved by the end of November. This early and fast retreat leads to a difference in ice
339 extent that can reach more than 10 million km² compared to the reference experiments at this time
340 and thus a sea ice extent corresponding to the one simulated only in early January in these reference
341 experiments (Fig. 2). The ThinIce experiments also display an earlier melting than ThickIce ones
342 because of a more efficient ice-albedo feedback, reinforcing the direct effect of the initially thinner ice
343 in winter. ~~This is due to a more efficient ice-albedo feedback:~~ it is easier to melt thin sea ice, leading
344 to a higher amount of open water and thus a larger absorption of incoming solar radiation and an
345 intensified melting.

346 *Minimum extent, subsequent advance season and amplitude of the seasonal cycle*

347 Experiments with earlier melt onset and larger melt rates show faster retreat and lower minimum
348 extent, leading to a larger difference between the experiments in the first summer than in the first
349 winter. In the experiments starting in March, the range of ice extent across all experiments at the first
350 maximum reaches 1.2 million km² for NEMO and 1.9 million km² for PARASO. For the following
351 minimum in the same experiments, it reaches 3.6 million km² and 3.8 million km², respectively. The
352 numbers for the summer minimum are relatively similar for the experiments starting in September
353 compared to those starting in March, which suggests that processes in the summer season are more
354 important than the state of the sea ice-ocean-atmosphere system in September (Tables 2 and 3).

355 By contrast, the state of the sea ice-ocean-atmosphere system in March (i.e. the second year for
356 the experiments starting in March but already the first year for the experiments starting in September)
357 has a dominant influence during the whole sea ice advance season (Marchi et al., 2020). Despite the
358 strong control from the insolation and the limited direct impact of sea ice physics and feedbacks with
359 the ocean and the atmosphere during the first advance season (see above), the model physics
360 influences thus the evolution of the sea ice extent for several months during the second advance
361 season through their effect on the state of the system in March. This is illustrated in Fig. 5b by the
362 association between positive minimum sea ice extent anomaly and the subsequent positive maximum
363 extent anomalies present in most experiments, with the notable exception of NoIceDyn experiments
364 as discussed below. In this figure, the minimum sea ice extent is chosen as a proxy for the state of the
365 sea ice and ocean system in summer but a similar link can be found for other variables, such as the
366 mean summer sea surface temperature southward of 60°S (Fig. S2S4).

367 The role of the state of the system in March can be illustrated for example using the Mix100
368 experiments. Increasing the vertical oceanic mixing in the sensitivity experiments redistributes the
369 available energy over the top 100 meters without modifying the vertically integrated heat content.
370 This does not have a large influence initially in the experiments starting in March (Fig. 2a). However,
371 the second year in the experiments starting in March is different from the first year as a deeper mixed
372 layer allows a larger heat uptake in summer. Consequently, the Mix100 experiments tend to have a
373 smaller ice extent than the reference experiments during the second sea ice advance season (Fig. 2a
374 and Fig. S1).

375 More generally, for both the coupled and uncoupled experiments, the summer extent influences
376 the whole advance season and the maximum extent. However, the difference in sea ice extent
377 between the experiments with NEMO tends to decrease with time because of the restoring imposed

378 by a fixed atmospheric state. For instance, the range in the maximum extent for the second year of the
379 experiments beginning in March reaches 2.1 million km² while it was 3.6 million km² the previous
380 summer (Fig. 2a). By contrast, the range between experiments increases during the sea ice advance
381 season in the PARASO experiments, reaching 4.8 million km² for the maximum extent in winter (25%
382 more than for the summer minimum).

383 While the majority of the experiments displaying a large winter ice extent also have a larger
384 summer ice extent, inducing relatively modest changes in the amplitude of the seasonal cycle, this is
385 not the case in the NolceDyn experiments. Those experiments are characterized by a reduced
386 amplitude of the seasonal cycle of the sea ice extent, with a smaller extent in winter and a larger one
387 in summer compared to the reference experiments. At the end of the advance season, the ice edge
388 position is set by the advection of sea ice from the south. Sea ice then melts in regions which are too
389 warm to sustain local production (e.g., Holland and Kimura, 2016; Nie et al., 2022). Neglecting ice
390 transport thus leads to an earlier maximum extent and onset of the retreat (Fig. 2). Later during the
391 retreat season, ice is transported northward where it melts and this transport also enhances the
392 formation of leads within the ice pack that increases solar absorption. Therefore, ice dynamics plays
393 an important role in accelerating the ice retreat, as shown in earlier studies (Fichefet and Morales
394 Maqueda, 1997; Holland and Kimura, 2016, Kusahara et al., 2019; Eayrs et al., 2020), and neglecting
395 this effect in NolceDyn induces an increase in the minimum ice extent of several million km² (Tables 2
396 and 3).

397 *Sensitivity to the starting date in NoMassFlux*

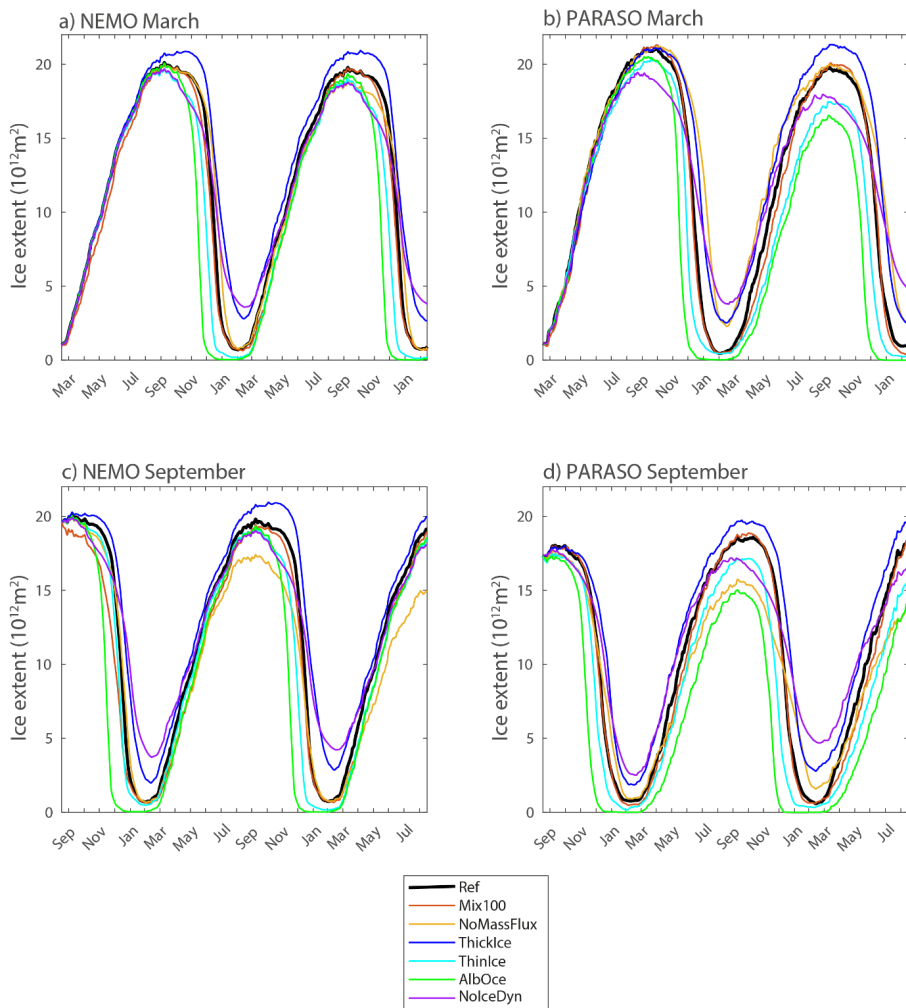
398 Neglecting brine release during ice formation (experiments NoMassFlux) reduces the heat input
399 from the deeper oceanic layer to the surface and results in a clear increase in ice production and
400 volume in the experiments started in March (Fig. 4), in particular in coupled mode. It only has a limited
401 influence on the sea ice extent during the first winter as, by definition, it can only act after sea ice is
402 already present (Martinson, 1990) (Fig. 2). The effect can only be seen indirectly during the sea ice
403 retreat season (when entrainment no longer plays a clear direct role) and the second year, through
404 the influence of the perturbation on the sea ice volume. In particular, this leads to an increase in sea
405 ice extent in NoMassFlux_PARA_Mar of nearly 2.0 million km² compared with the corresponding
406 reference experiment in summer (Fig. 2 and Fig. S1).

407 The NoMassFlux experiments starting in September have a different behavior than the
408 experiments beginning in March. As the model has a very low sea ice volume in March, assuming that
409 sea ice has the same salinity as the ocean does not substantially impact the salt and freshwater balance
410 of the model. In contrast, for the experiments starting in September, because of the much larger initial
411 sea ice volume, the NoMassFlux experiments imply a large artificial salt input in the system. The salt
412 input weakens the upper ocean stratification, enhances mixing and triggers open ocean convection
413 and the formation of open ocean polynyas (Fig. 6). This brings a large amount of heat to the ocean
414 surface, reducing both the sea ice volume and winter sea ice extent in NoMassFlux_NEMO_Sep and
415 NoMassFlux_Par_Sep compared with the corresponding reference experiments.

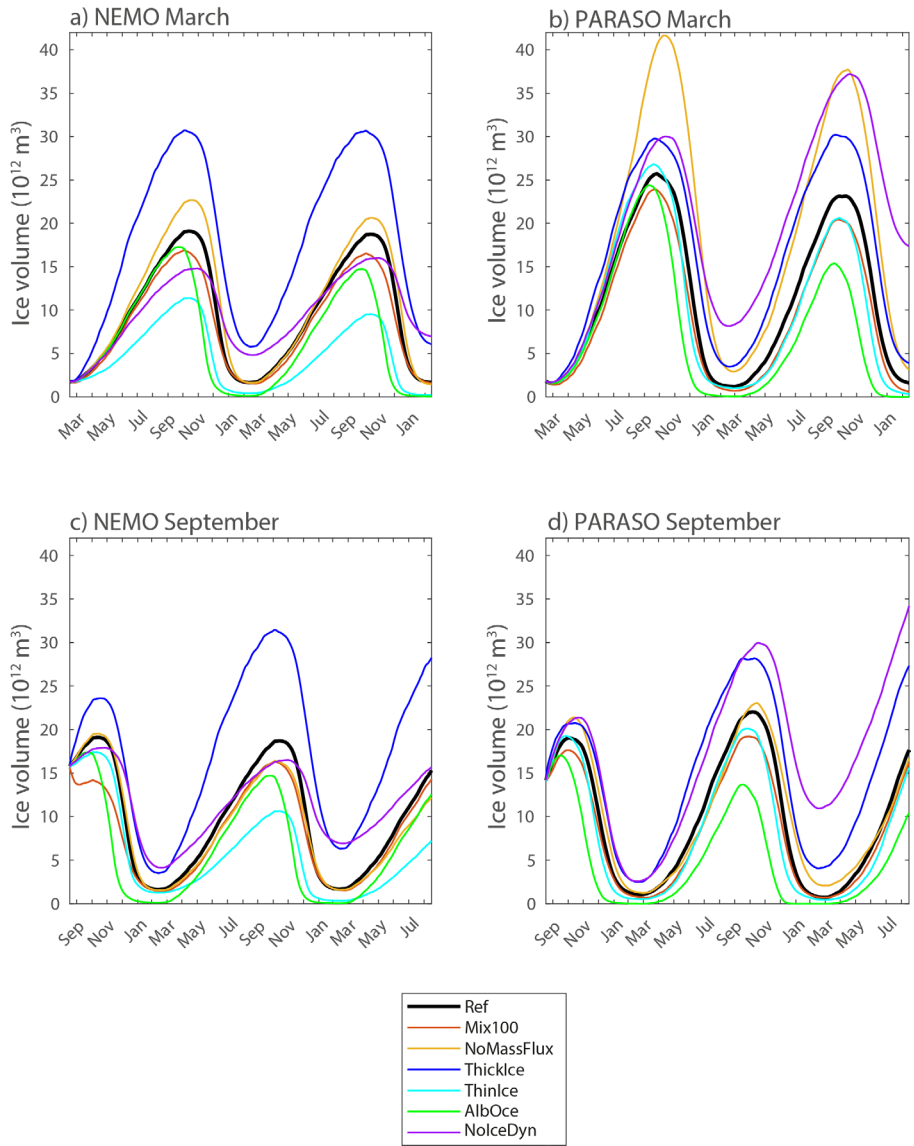
416 *Timing of the maximum and minimum extents*

417 Overall, as expected based on previous studies, the effect of the perturbations prescribed in our
418 sensitivity experiments is relatively modest on the timing of the minimum and maximum ice extents.
419 The largest signal arises in the sea ice dynamics perturbation, which tends to advance the date of
420 maximum in the coupled experiments (14 days and 12 days for the second maximum in
421 NolceDyn_PAR_Mar and NolceDyn_PAR_Sep, respectively), and in the experiment with perturbed
422 heat conduction, as the thicker pack can delay the maximum by up to 25 days (in ThickeNEMO_Sep).

423 Open ocean convection can also bring forward the date of the maximum with a third maximum already
 424 achieved in day 230 and day 239 the second year in NoMassFlux_NEMO_Sep and
 425 NoMassFlux_PAR_Sep (36 and 28 days earlier compared to the previous year of the same experiment,
 426 respectively). The summer minimum can be advanced by up to 43 days in AlbOce_PAR_Sep through
 427 the albedo decrease, and delayed by up to 18 days in the sea-ice dynamics deprived experiment
 428 NoIceDyn_NEMO_Sep. Note that some values in Tables 2 and 3 should be taken with caution as the
 429 evolution of sea ice extent is relatively flat close to the maximum and small differences can produce
 430 large shifts in the specific day of the maximum (e.g. in Mix100_PAR_Sep and ThinIce_PAR_Sep).

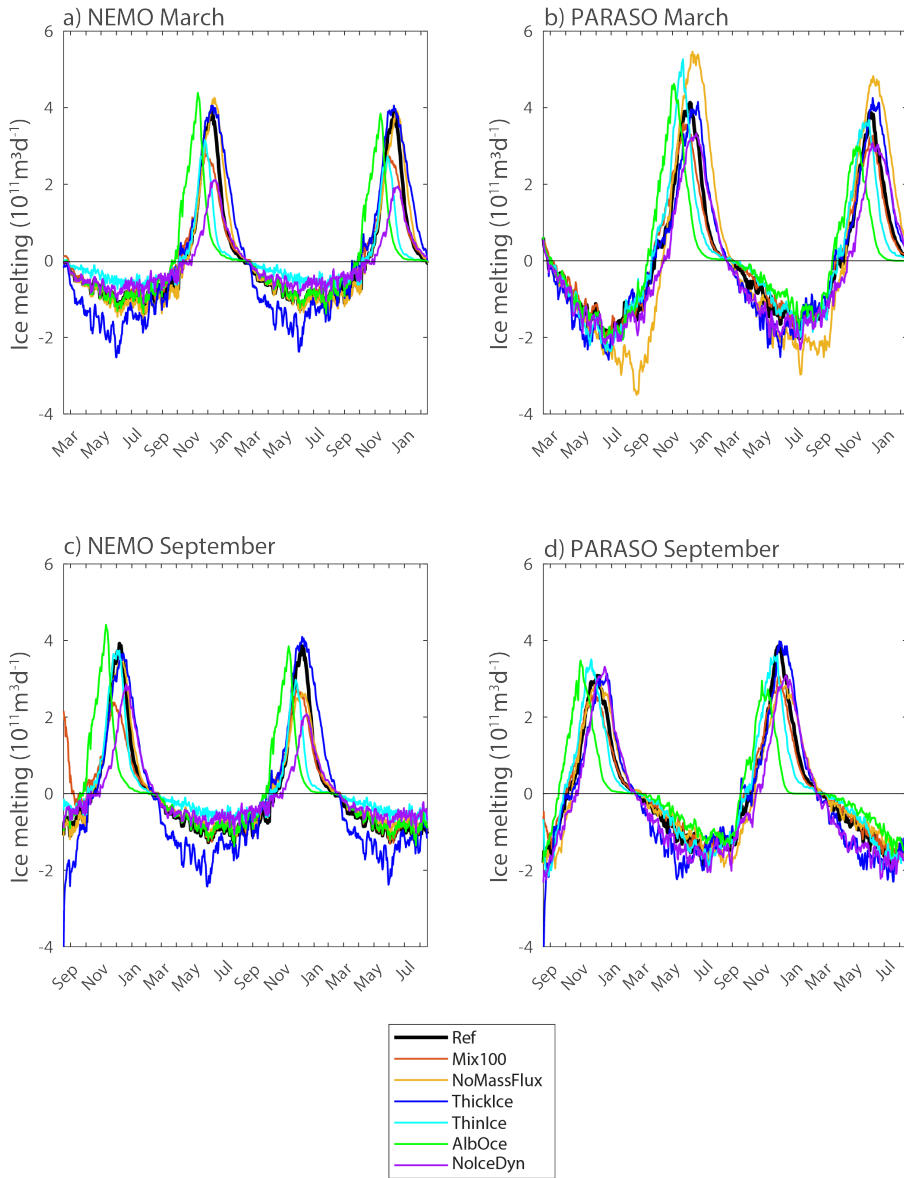


431
 432 Figure 2. Antarctic sea ice extent (in 10^{12} m^2) in the group of experiments starting in March
 433 (top row) and September (bottom) for the NEMO (left column) and PARASO configurations
 434 (right column). The equivalent figure showing the anomaly compared to the corresponding
 435 reference simulation is provided in Fig. S1.
 436



437
 438
 439
 440

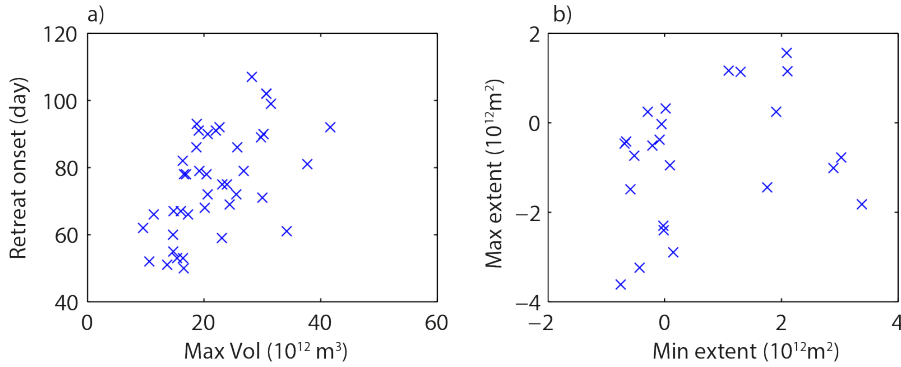
Figure 3. Antarctic sea ice volume (in 10^{12} m^3) in the group of experiments starting in March (top row) and September (bottom) for the NEMO (left column) and PARASO configurations (right column).



441

442 Figure 4. Mass flux due to sea ice growth and melt (counted positive for melting) integrated over
 443 the Southern Ocean (in $10^{11} \text{ m}^3 \text{ d}^{-1}$) in the group of experiments starting in March (top row) and
 444 September (bottom) for the NEMO (left column) and PARASO configurations (right column). This
 445 diagnostic is evaluated online in NEMO from the different contributions to ice formation and melting
 446 but is equivalent to the time derivative of the ice volume. The equivalent figure showing the anomaly
 447 compared to the corresponding reference simulation is provided in Fig. S2.

448



449

450 Figure 5. a) Onset of significant seasonal sea ice retreat (in day), defined as the number of days
 451 after the maximum at which the Antarctic sea ice extent has decreased to 95% of its maximum value
 452 as a function of the maximum ice volume (in 10^{12} m^3). b) Maximum sea ice extent anomaly (in 10^{12} m^2)
 453 compared to the reference experiment as a function of the anomaly in the previous minimum (in
 454 10^{12} m^2) for the second year of the experiments starting in March and for the first minimum and second
 455 maximum of the experiments starting in September.

456

457 Table 2. Values and timings of the maximum and minimum sea ice extents for the two years of the
 458 sensitivity experiments starting in March. Extents are given in 10^{12} m^2 and timings in Julian days.

	Year 1				Year 2			
	Max	Min	Day Max	Day Min	Max	Min	Day Max	Day Min
Ref_NEMO_Mar	20.1	0.70	265	46	19.8	0.73	266	47
Mix100_NEMO_Mar	20.0	0.64	265	57	19.8	0.66	266	57
NoMassFlux_NEMO_Mar	20.0	0.79	265	46	18.8	0.70	266	49
ThickIce_NEMO_Mar	20.9	2.80	265	58	20.9	2.66	291	58
ThinIce_NEMO_Mar	19.7	0.17	265	48	19.0	0.12	266	47
NolceDyn_NEMO_Mar	19.7	3.59	265	59	18.8	3.58	266	60
AlbOce_NEMO_Mar	20.1	0.03	265	43	19.4	0.01	266	43
Ref_PAR_Mar	21.1	0.45	269	48	19.8	0.59	267	60
Mix100_PARA_Mar	21.3	0.46	286	48	20.1	0.37	269	57
NoMassFlux_PARA_Mar	21.2	2.36	294	59	20.0	2.29	267	63
ThickIce_PARA_Mar	21.1	2.54	294	59	21.3	2.45	267	59
ThinIce_PARA_Mar	20.3	0.42	276	48	17.5	0.23	264	50
NolceDyn_PARA_Mar	19.4	3.82	249	59	17.9	3.79	253	65
AlbOce_PARA_Mar	20.5	0.02	269	57	16.5	0.00	265	30

459

460

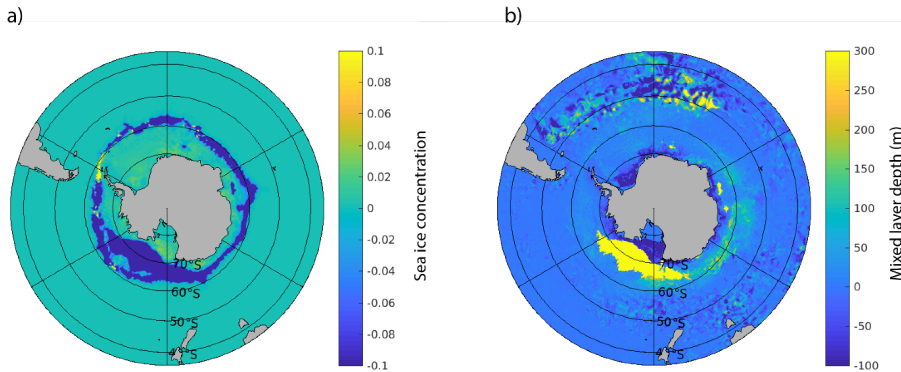
461

462

463 Table 3. Values and timings of the maximum and minimum sea ice extents for the two years of the
 464 sensitivity experiments starting in September. Extents are given in 10^{12} m^2 and timings in Julian days.

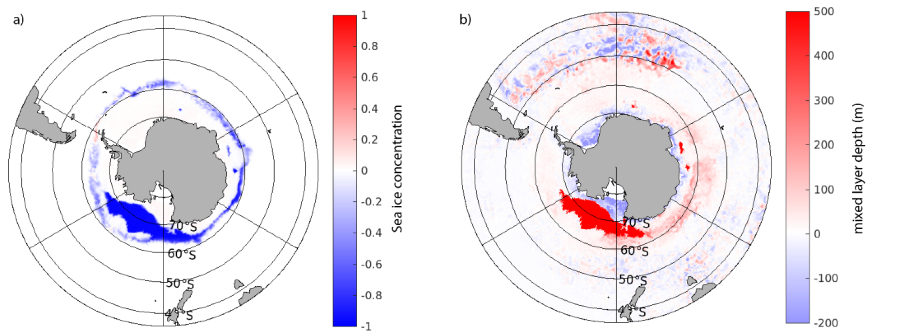
	Year 1				Year 2			
	Max	Min	Day Max	Day Min	Max	Min	Day Max	Day Min
Ref_NEMO_Sep	20.1	0.69	265	44	19.8	0.73	266	45
Mix100_NEMO_Sep	19.6	0.60	244	57	19.4	0.66	266	55
NoMassFlux_NEMO_Sep	19.9	0.67	265	49	17.4	0.69	266	47
ThickIce_NEMO_Sep	20.3	1.99	265	57	20.9	2.66	286	56
ThinIce_NEMO_Sep	20.0	0.48	265	44	19.3	0.12	266	44
NoIcDyn_NEMO_Sep	20.0	3.71	265	59	19.0	3.58	266	63
AlbOce_NEMO_Sep	20.0	0.03	265	44	19.3	0.01	266	41
Ref_PARA_Sep	18.0	0.76	268	56	18.6	0.58	267	58
Mix100_PARA_Sep	18.0	0.46	269	50	18.9	0.61	290	56
NoMassFlux_PARA_Sep	17.7	0.90	262	57	15.7	1.58	267	58
ThickIce_PARA_Sep	18.0	1.85	287	61	19.8	2.78	275	58
ThinIce_PARA_Sep	17.5	0.16	269	47	17.2	0.32	289	54
NoIcDyn_PARA_Sep	17.8	2.52	262	63	17.2	4.68	255	65
AlbOce_PARA_Sep	17.4	0.00	244	64	15.0	0.00	267	15

465



Mis en forme : Centré

466



467

468 Figure 6. Differences in a) ice concentration and b) mixed layer depth (in m) in August of the second
 469 year of simulation between NoMassFlux_NEMO_Sep and the corresponding reference experiment.

470

471 **4 Atmospheric feedbacks**

472 The results discussed in Section 3 have highlighted differences between the NEMO and PARASO
 473 experiments and the role of the coupling with the atmosphere is further quantified here. In NEMO, the
 474 surface energy budget has only one degree of freedom (the surface temperature). Therefore, the
 475 surface readily adjusts to the forcing, so that the surface temperature closely follows the air
 476 temperature, which can be seen as a form of restoring. In PARASO, the surface energy budget responds
 477 to both sea ice and atmospheric processes. Another degree of freedom is now that the atmosphere
 478 warms or cools in response to changes in sea ice, which in turn affects non-solar (downward longwave
 479 and turbulent) fluxes.

480 This effect of the changes in the atmosphere is evaluated by computing atmospheric feedback
 481 factors in response to the perturbation for each pair of coupled and uncoupled model experiments.
 482 Feedbacks can be evaluated in different ways. A methodology that is consistent for a wide range of
 483 feedbacks, including the standard radiative ones involved in computation of the so-called climate
 484 sensitivity as well as non-radiative feedbacks, is to define the feedback factor γ_{as} (Goosse et al., 2018):

$$485 \quad \gamma = \frac{\textit{Total Response} - \textit{Reference Response}}{\textit{Total Response}} \quad (1)$$

486 where the *Total Response* corresponds to the response of the model to some perturbation imposed in
 487 the system when all the feedbacks are active, while the *Reference Response* is the response of the
 488 model to the same imposed perturbation when one feedback or process to be studied (for instance
 489 sea ice dynamics) has been left out. As our specific goal is to study the impact of atmospheric coupling,
 490 this leads to:

$$491 \quad \gamma = \frac{\textit{Coupled Response} - \textit{Uncoupled Response}}{\textit{Coupled Response}} \quad (2)$$

492 and for sea ice extent specifically:

$$493 \quad \gamma_{SIE} = \frac{\Delta SIE_{PARA} - \Delta SIE_{NEMO}}{\Delta SIE_{PARA}} \quad (3)$$

494 where ΔSIE_{PARA} and ΔSIE_{NEMO} are the changes between the sensitivity experiments and the reference
 495 experiments in the PARASO and NEMO configurations, respectively.

496 The feedback factor can be related to the feedback gain G (e.g., Goosse et al. 2018) defined here
 497 as the ratio between the response in coupled mode and the one in uncoupled mode:

$$498 \quad G = \frac{\Delta SIE_{PARA}}{\Delta SIE_{NEMO}} = \frac{1}{1 - \gamma_{SIE}} \quad (4)$$

499 A negative value of γ thus corresponds to a negative feedback (changes in PARASO smaller than in
 500 NEMO, feedback gain smaller than 1, and the feedback dampens the response to a perturbation); a
 501 value between 0 and 1 corresponds to a positive feedback (changes in PARASO larger than in NEMO,
 502 feedback gain larger than 1, the feedback amplifies the perturbation); a value of 1 implies an infinite

503 gain and values of γ larger than 1 imply a change in the sign of the response between coupled and
504 uncoupled model experiments (negative feedback gain). In the following, we start by discussing the
505 feedback factors lower than 1 (positive and negative feedbacks and positive feedback gains) that are
506 the easiest to interpret in a linear framework, while non-linearities and values of γ larger than one
507 (negative feedback gain) will be discussed in the last paragraphs of the section. We must recall here
508 that we were not able to perform ensembles of simulations for our sensitivity experiments, leading to
509 some uncertainties in the evaluation of the model response to the perturbations and thus in the
510 estimate of the feedback parameters. Consequently, we ~~We~~ have not analyzed the feedback factors
511 when the coupled response is smaller than 0.2 million km² for sea ice extent or 0.2 thousand km³ for
512 sea ice volume, corresponding to very small changes in the system and large feedback factors (the
513 coupled response appears in the denominator of γ). Consistently, we have focused the analyses on the
514 second year of the experiments, as for the first year the changes in several experiments are too small.
515 Nevertheless, even with those criteria, the small model internal variability has still an influence on the
516 estimate of the feedback parameters and, in particular, it may also contribute to the non-linearities
517 and values of γ larger than one discussed below.

Mis en forme : Couleur de police : Automatique

Mis en forme : Couleur de police : Automatique

Mis en forme : Couleur de police : Automatique

518

519 *Atmospheric feedbacks on the maximum ice extent.*

520 The feedback factors are always positive for the maximum sea ice extent (Fig. 7a), indicating that
521 the coupling with the atmosphere amplifies the wintertime response to perturbations (for the
522 feedback factors smaller than 1, for the ones larger than 1 see below). This matches well our
523 understanding of the system, where sea ice acts as an insulator between the atmosphere and the
524 ocean. An increase in sea ice extent resulting from a perturbation thus cools the atmosphere, which
525 amplifies the initial change, giving a positive feedback. The same positive feedback mechanism applies
526 in the context of an initial decrease in ice extent, leading to atmospheric warming and additional
527 decrease in extent. For example, in AlbOce_PARA_Mar, the surface air temperature is higher than in
528 the reference experiment all year long. The difference reaches 1.5K on average over the two years of
529 the simulations for the oceanic region south of 60°S, and more than 2.5K in the second winter (Fig. 8,
530 Fig. ~~S55~~).

531 Among all the experiments, AlbOce displays the largest feedback gain for the winter ice extent
532 (i.e. $\gamma < 1$ and closest to 1), with values of $\gamma = 0.87$ (Fig. 7a) in both experiments started in March and
533 September and hence a feedback gain of 7.7 (Fig. ~~S4a~~~~S6a~~). This is not surprising as the albedo changes
534 associated to sea ice variations are usually considered as a key characteristic of polar marine climates.
535 The sea-ice albedo feedback is already active in the NEMO configuration as a change in sea-ice
536 concentration affects the surface albedo and thus the net solar radiation absorbed at surface: in
537 AlbOce_NEMO_Mar and AlbOce_NEMO_Sep, the ocean-sea ice surface south of 60 S have a net solar
538 absorption higher than in their reference counterparts of 13 W m⁻² in annual mean (Fig. ~~S57~~). This
539 is even higher than in AlbOce_PARA_Mar and AlbOce_PARA_Sep, where the change reaches only
540 7 W m⁻². The higher values in the NEMO configuration might be due to differences in the mean state
541 between the coupled and uncoupled model configurations or to feedbacks related to clouds in
542 PARASO, but investigating those effects in more detail is out of the scope of the present study.
543 Nevertheless, the main difference between the coupled and uncoupled experiments comes from the
544 non-solar heat fluxes (Fig. ~~S68~~), which is the net downward flux associated with incoming and
545 outgoing longwave radiation, and latent and sensible heat exchange with the atmosphere. In
546 AlbOce_NEMO_Mar and AlbOce_NEMO_Sep, as the atmospheric state is prescribed, the reduction in
547 sea ice extent and surface warming induce a large increase in non-solar heat losses that reaches 10

548 and 13 Wm^{-2} averaged over the area south of 60°S , respectively. In other words, the artificial restoring
549 to the observed atmospheric state in uncoupled mode makes the non-solar heat loss at the surface
550 nearly compensate for the additional solar heat input. By contrast, the atmospheric warming in
551 AlbOce_PARA_Mar and AlbOce_PARA_Sep only leads to a moderate increase of the non-solar heat
552 losses, with annual mean values of 1 and 4 Wm^{-2} , respectively. This explains the larger changes in ice
553 extent in coupled mode (Fig. 2) and the strong drift of the system to a warmer state (Fig. 8).

554 *Atmospheric feedbacks on maximum ice volume.*

555 The feedback factor for the winter volume is also positive in many experiments (Fig. 7b). In
556 particular, the value of γ in NoMassFlux_Mar equals 0.87, corresponding to a feedback gain G of 7.7.
557 In NoMassFlux experiments, the heat input from the ocean to the surface is reduced because of the
558 absence of the ice production–entrainment feedback. This increases ice production and thus ice
559 thickness. In the coupled model integration, the downward non-solar (net LW and turbulent) fluxes
560 can respond to thicker ice and colder surface, which further decreases the surface air temperature by
561 more than 3K on average over the oceanic region south of 60°S during the sea ice growth season.
562 This cooling further enhances the ice production and leads then to a very strong positive atmospheric
563 feedback.

564 By contrast, the atmosphere provides a negative feedback in the case of the ThinIce and ThickIce
565 experiments. Larger snow and ice thermal conductivities in ThickIce imply larger heat losses from the
566 ocean to the atmosphere in ice-covered regions and thus larger winter sea ice production in all the
567 ThickIce experiments (Fig. 4). In the PARASO configuration, the increased heat conduction from the
568 ice-ocean system warms the lower atmosphere in winter within the ice pack by more than 3K ,
569 integrating over the region south of 60°S (Fig. 8). Consequently, the non-solar atmosphere-ice heat
570 fluxes can increase in coupled mode, moderating the increase in sea ice volume compared to the
571 NEMO experiments. In ThinIce, the smaller heat conduction fluxes tend to induce an atmospheric
572 cooling in winter but this effect is not strong enough to decrease the temperature in the majority of
573 regions, likely because of a dominant effect of the albedo reduction in this experiment. However, a
574 cooling is still found close to the continent (Fig. S5). As this is the region where the largest changes in
575 sea ice thickness occur compared to the reference experiment, this dominates the effect of the
576 coupling on the total ice volume. (For more information on the difference between the temperature
577 responses in ThickIce and ThinIce, see the supplementary discussion).~~In ThinIce, the smaller heat~~
578 ~~conduction fluxes induce an atmospheric cooling in winter, located mainly close to the continent~~
579 ~~where the largest volume change occurs compared to the reference experiment.~~

580 The experimental design in ThickIce and ThinIce may appear counterintuitive as our modifications
581 to the model physics warm the atmosphere when the ice is thicker. Such perturbations highlight a
582 coupling between heat conduction in the ice and non-solar downward atmospheric heat fluxes. When
583 the full system is considered in the real world, we rather experience the effects of the strong coupling
584 between thickness and heat conduction, often referred to as the ice growth-thickness feedback in
585 which an anomalously thin sea ice cover will lose more energy by conduction in winter, leading to a
586 thicker and colder ice, reducing the initial anomaly (Maykut, 1986; Bitz and Roe, 2004; Goosse et al.,
587 2018).

588 *Atmospheric feedbacks on minimum ice extent and volume.*

589 Positive feedback factors associated to the coupling with the atmosphere would also be expected
590 for the minimum ice extent (Fig 7c), in particular because of the amplifying role of the ice-albedo
591 feedback and its impact on air temperature. This interpretation is consistent with the highest summer
592 air temperature in the two experiments with the lowest summer ice extent (ThinIce and AlbOce, Fig.

Mis en forme : Couleur de police : Automatique

593 8). Accordingly, positive values are found in several experiments. However, negative values are also
594 obtained for others. ~~This~~ Those positive values may be surprising in particular for AlbOce but this can
595 be considered as an artefact related to the methodology used to compute γ . All the sea ice melts in
596 summer in the experiments AlbOce (Figs. 2 and 3). The response is thus equal to the summer sea ice
597 extent (or volume) in the corresponding reference experiments. As this reference extent (and volume)
598 is slightly higher in NEMO configuration than in PARASO (Figs. 1 and 2), the response is larger in NEMO.
599 ~~This then leads leading~~ to a negative value of γ by definition (Eq. 3).

600 For ThinIce and ThickIce experiments, the negative atmospheric feedback factors obtained for the
601 summer ice volume (Fig 7d) are a direct consequence of the negative values discussed above for winter
602 ice volume in the same experiments, the winter sea ice thickness anomalies persisting until the
603 summer. As those anomalies are particularly large close to the coast, they affect the melting in those
604 regions and thus the feedback factor for the summer sea ice extent, leading to a negative value in
605 ThinIce and values very close to zero in the ThickIce experiments (Fig. 7c).

606 *Feedback factors larger than one: impact of the spatial distribution of the response.*

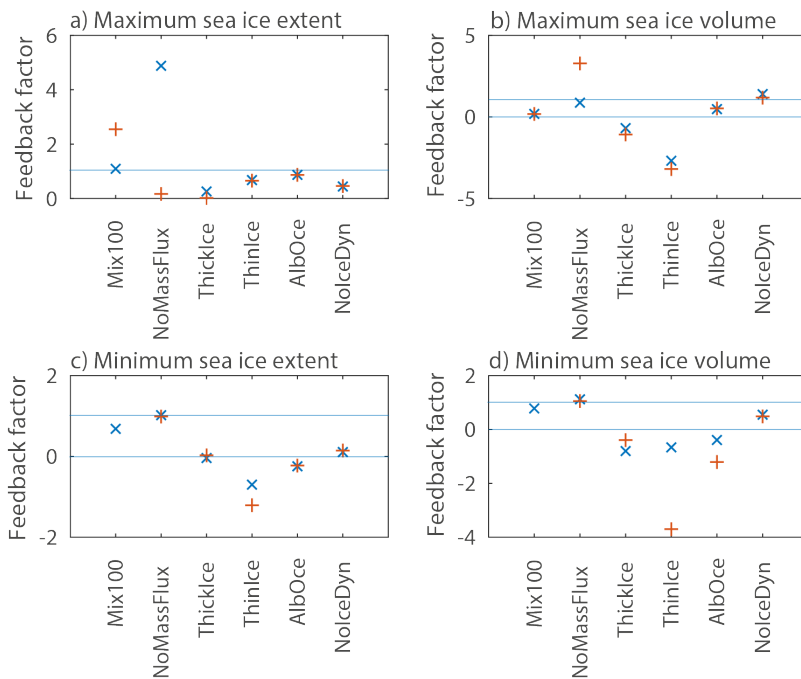
607 The analyses of the feedback factors illustrate the nonlinearity of the system, for example when
608 comparing the very different values of γ for an increase or a decrease in the conductivity in ThickIce
609 and ThinIce. Values of γ higher than one also suggest more complex dynamics than a simple
610 amplification or damping of the response by interactions with the atmosphere as even the sign of the
611 response is different between coupled and uncoupled model configurations. In many cases, this
612 different sign of the response integrated over the whole Southern Ocean, as measured on the anomaly
613 of total sea ice extent or ice volume, is due to a spatially heterogenous response in uncoupled mode.
614 The coupling amplifies or damps the response locally as described by the feedback framework.
615 However, this may change the balance between positive and negative contributions and thus modify
616 the sign of the response integrated over the whole Southern Ocean compared to the uncoupled mode,
617 explaining the value of γ higher than 1.

618 We will not discuss here all the experiments displaying a value of γ higher than 1, especially
619 because in some cases the difference in the response to the coupling is small and thus probably not
620 very meaningful. Nevertheless, two examples seem illustrative and are detailed below. In NolceDyn,
621 the sea ice thickness increases in winter close to the coast and decreases close to the ice edge
622 compared to the reference experiment, both in coupled and uncoupled mode (Fig. ~~S7S9~~). The
623 integrated volume response is thus a balance between the changes in the two regions and, depending
624 on their relative strength, the sign of the change in ice volume can change. In coupled mode, the very
625 large increase in thickness close to the coast associated with strong local positive feedbacks with the
626 atmosphere dominates, while in the uncoupled mode, the offshore decrease dominates, then leading
627 to γ greater than 1 for winter ice volume.

628 At the time of the winter maximum in sea ice extent, sea ice is transported to the ice edge where
629 it tends to melt. The associated freshwater release increases the upper ocean stratification in the
630 reference experiment, reducing the oceanic heat input to the surface ~~and~~ thus favoring the advance
631 of the pack. (This positive feedback at the ice edge at the time of the maximum ice extent can be
632 contrasted with the negative ice production-entrainment feedback within the pack). In
633 NoMassFlux_NEMO_Mar, the absence of freshwater release during ice melt leads to a weaker upper
634 ocean stratification close to the ice edge, allowing deeper mixed layers, with a difference that can
635 reach more than 100m. As a consequence, the heat input from the ocean to the ice is higher. This is
636 sufficient to limit the seasonal sea ice advance and the maximum ice extent is lower in
637 NoMassFlux_NEMO_Mar than in the reference experiment by about 1 million km² in the second year

638 of the experiments (Fig. 2a). By contrast, the large increase in ice thickness and volume in
 639 NoMassFlux_PARA_Mar discussed previously dominates the response even at the ice edge, leading to
 640 a positive anomaly in the maximum ice extent. As a consequence, the atmospheric feedback factor is
 641 greater than one. This effect is only seen in the experiments starting in March, as those starting in
 642 September are dominated by the consequences of deep mixing and polynya formation within the pack.

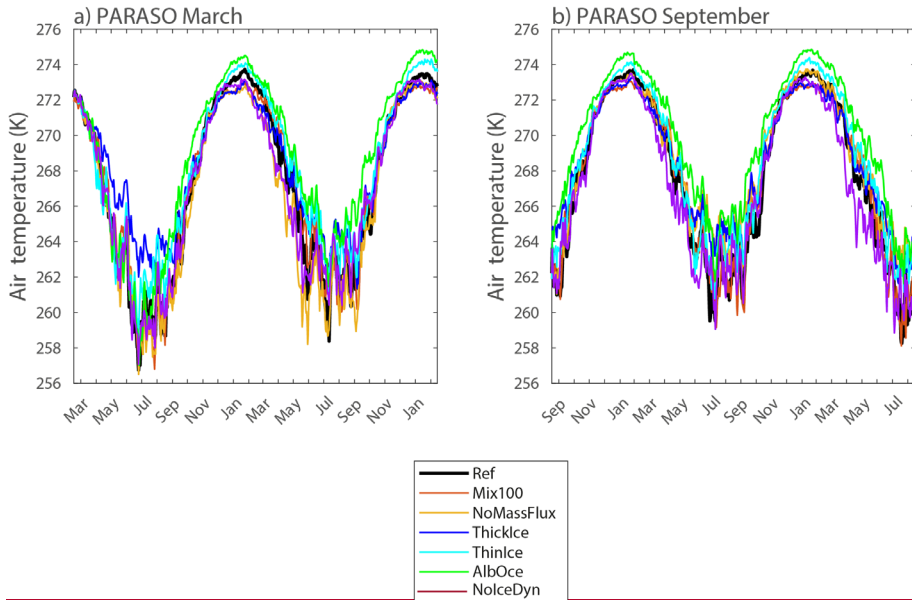
643



644

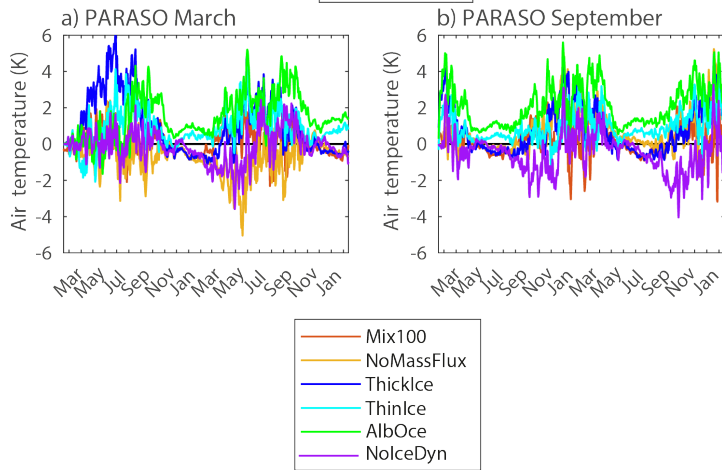
645 Figure 7. Atmospheric feedback factor for experiments starting in March (blue x) and September
 646 (red +) for a) the maximum sea ice extent, b) maximum sea ice volume, c) minimum sea ice extent and
 647 d) minimum sea ice volume. Light blue lines are drawn at values of 0 and 1 (with positive feedback
 648 between those two lines). The equivalent figure for the feedback gain G is given as Fig. [S4S6](#).

649



Mis en forme : Centré

650



651

652 Figure 8. Anomaly of S_s surface air temperature (in K) averaged over the oceanic region south of
 653 60°S compared to the corresponding reference simulation in the group of experiments starting a) in
 654 March and b) in September for the PARASO configuration.

655

656 5 Discussion and conclusions

657 We have performed a series of 24 sensitivity experiments to analyze the role of key-sea ice
 658 processes and coupling mechanisms between sea ice, ocean and atmosphere in driving the seasonal
 659 cycle of the Antarctic sea ice extent. In order to obtain clear signals and identify the mechanisms at
 660 play, deliberately strong and idealized perturbations have been used in our simulations. One limiting

661 aspect arising from making such a design choice is the resulting lack of ability to directly compare the
662 experiments with observational datasets. Furthermore, our quantitative results may be model-
663 dependent, as they can be influenced by the way physical processes are represented in the models
664 and by the biases in the model mean state, which can have a strong influence on the response of
665 models to perturbations (e.g. Goosse et al., 2018; Massonnet et al., 2018). Additionally, the
666 experimental design itself may have an impact on the way some of the processes are evaluated.
667 However, we consider that the relative importance of the different processes and their description are
668 robust and we will thus focus on those aspects here.

669 Recall that all the simulations used the same atmospheric forcing (for NEMO simulations) or the
670 same conditions at the boundaries of the domain of the regional atmospheric model that significantly
671 constrain the seasonal evolution of the sea ice (PARASO simulations). Changes in the large-scale
672 atmospheric conditions or in the passage of synoptic storms close to the ice edge, ~~for instance,~~ are
673 known to have a strong impact on the evolution of the ice extent (e.g., Handcock and Raphael, 2020).
674 While this role of the atmospheric variability is not addressed here, the analyses of the processes at
675 play could provide insight for understanding how the ice-ocean system responds to interannual
676 variations of the atmospheric conditions. In particular, our results are consistent with the large role
677 attributed to the sea ice dynamics, and thus to the interannual variability in winds, in driving sea ice
678 extent anomalies during the retreat season (e.g., Holland 2014; Kushara et al., 2019; Eayrs et al., 2020)
679 as well as with the impact of changes in spring on the sea ice extent trends observed in autumn
680 (Holland 2014). For instance, our results are consistent with the large role attributed to the sea ice
681 dynamics and thus to the interannual variability in winds in driving changes in sea ice extent anomalies
682 during the retreat season (e.g., Kushara et al., 2019; Eayrs et al., 2020). Conversely, the magnitude and
683 relative importance of the different processes and feedbacks investigated in this study may vary from
684 one year to another, as a function of the state of the system or of the large-scale forcing (e.g., Goosse
685 et al. 2018). It would thus be instructive to repeat the analyses performed here for various years and
686 conditions to determine how this affects the value of the feedback parameters.

Mis en forme : Couleur de police : Automatique

Mis en forme : Couleur de police : Automatique

687 Our experiments are too idealized to provide explicit recommendations for model improvements
688 but the identification of the key processes can help to target the changes that might have the largest
689 impact. In particular, the delayed onset of the seasonal sea ice retreat after the maximum present in
690 our simulations can possibly be related to a too thick ice cover close to the winter ice edge, which may
691 be associated with a misrepresentation of processes in the marginal ice zone (Roach et al., 2018, 2019;
692 Alberello et al., 2020; Horvat, 2021). Additionally, the too fast ice retreat in our control runs is likely
693 impacted by the model biases in the sea ice transport because of the dominant role of this process
694 during spring (Holland and Kwok 2012; Lecomte et al. 2016; Kushara et al., 2019; Eayrs et al., 2020,
695 Sun and Eisenman 2021).

696 We have focused on the sea ice extent integrated over the whole Southern Ocean, although the
697 net influence of a process may be the result of opposite effects between sectors of the Southern Ocean
698 or between coastal regions and the open ocean. For instance, removing ice dynamics tends to increase
699 the ice thickness close to the coast and decrease it at the sea ice edge because of a reduced ice
700 transport, with a clear impact on the temperature changes. This is an illustration that our conclusions
701 derived for the whole ice pack are not necessarily valid for a specific region.

702 Overall, our results confirm the earlier finding that the model physics have only a moderate effect
703 on the timings of the maximum and minimum Antarctic sea ice extents, which are rather controlled by
704 the insolation cycle (Roach et al., 2022). Deactivating the sea ice dynamics in our models induces an
705 earlier maximum and a tendency towards a later minimum, but the shift is at maximum of the order
706 of one week or two, which is within the range of year-to-year fluctuations in the observed record.

707 Thicker ice can delay the maximum and a lower albedo lead to an earlier minimum, but similarly this
708 does not strongly modify the shape of the seasonal cycle, in particular its asymmetry. Our experiments
709 are only 2 years in length and there is a possibility that the shifts would become larger at equilibrium,
710 but in the experiments featuring a clear drift (such as NoiceDyn_PAR and AlbOce_PAR), we observe a
711 change in the values of the maximum and minimum ice extents from the first to the second year rather
712 than on their timing. The only exception is related to strong open ocean convection that can stop the
713 ice advance season efficiently when it is triggered in the model.

714 Nevertheless, our results demonstrate that sea ice physics and interactions with the atmosphere
715 and ocean control many other aspects of the seasonal cycle of the ice extent, such as the values of the
716 maximum and minimum and the speed of the retreat. They thus strongly modulate the overall impact
717 of the sea ice in the climate system, in particular on the radiative balance through the modification of
718 the surface albedo and on the exchanges of heat and carbon between the ocean and atmosphere.

719 Our sensitivity experiments have also illustrated clear distinctions between the dynamics of the
720 sea ice advance and retreat seasons. The sea ice extent advance from March to August is nearly
721 insensitive to the perturbations applied, with nearly identical evolution of the sea ice extent in our
722 experiment over this period if they start from the same initial conditions in March. If the conditions
723 are different in March (e.g., inherited from differences during the previous melting season), this has
724 an effect during the whole advance season. We can interpret those results in the following way. The
725 very weak incoming solar radiation between March and August imposes a large heat loss over the
726 Southern Ocean and the response of the system depends more on the heat available in March (and
727 thus of conditions at that time) than on any other element in the system. However, the sea ice
728 processes during the ice advance season can have an indirect effect by changing the sea ice thickness
729 and modifying the sea ice extent later in the year. This is the case for the ice production-entrainment
730 feedback that limits the ice growth in winter. During the ice advance season, this has no major impact
731 on the ice extent itself as it modulates the characteristics of sea ice that is already present, but the
732 modification of the thickness has an influence later during the retreat.

733 The timing of the beginning of the seasonal sea ice retreat and its rate also depend on the late
734 winter conditions, with thicker ice melting later. However, the retreat rate differs strongly between
735 the experiments, and this may have a larger impact on the spring and summer ice extents than the
736 conditions in September. Among all the processes influencing the retreat rate, the ice albedo feedback
737 is the dominant one, with a lower albedo, whether it is induced directly by a change in albedo (AlbOce)
738 or indirectly by a thinner ice (ThinIce) that melts faster, strongly accelerating the ice retreat. The ice
739 transport also plays a clear role by transporting sea ice northward where it melts. Neglecting this
740 process therefore leads to a large increase in summer ice extent. This larger dependence on several
741 key physical processes during the seasonal ice retreat is consistent with the larger climate model
742 sensitivity to changes in parameters in spring and early summer than during the ice advance season
743 (e.g., Urrego-Blanco et al., 2016; Schroeter and Sandery, 2022) and with the larger interannual
744 variability in the melt rates observed over the satellite period than in the growth rates (e.g., Eayrs et
745 al., 2020).

746 From a prediction point of view, the findings of this paper are also consistent with the idea that
747 the seasonal predictability of Antarctic sea ice extent depends on the season itself (Chevallier et al.,
748 2019; Marchi et al., 2020). A diagnostic predictability study using satellite data has revealed that
749 February is the month for which the sea ice extent anomalies exhibit the largest autocorrelations for
750 all lead times up to 55 days (Chevallier et al., 2019). This [higher autocorrelation for February](#) is in line
751 with our findings showing that the seasonal development of sea ice extent during the growing season
752 is minimally controlled by physics but rather by insolation and initial conditions. By contrast, the lowest

753 autocorrelations of sea ice extent anomalies are reached in the melting season, with complete loss of
754 predictability in mid-November. This is again in line with our results that multiple physical factors
755 control the dynamics of sea ice melt.

756 The impact of all the sea ice and oceanic processes investigated here on the ice extent in winter
757 are amplified by the coupling with the atmosphere and our experimental design allows us to quantify
758 this amplification. The largest winter atmospheric feedback occurs for perturbations in albedo, as this
759 strongly modifies atmospheric temperature and humidity, amplifying the response of the ice. The
760 effect of the ice production-entrainment feedback is also strongly amplified by the atmospheric
761 coupling, as it brings thermal energy to the surface that melts ice but also warm up the atmosphere,
762 increasing the response of sea ice. By contrast, negative atmospheric feedbacks can develop for the
763 ice thickness and volume. In particular, larger heat losses due to higher conductive heat fluxes through
764 the sea ice can lead to greater sea ice formation. This induces a larger thermal energy transfer from
765 the ice-ocean system to the atmosphere that reduces the initial heat loss, resulting in a negative
766 atmospheric feedback on the thickness and potentially on the summer extent.

767 Roach et al. (2022) identified the role of insolation in controlling the observed asymmetry in the
768 growing and melting of Antarctic sea ice. Our idealized sensitivity experiments show that within this
769 robust cycle, the melt rate and maximum and minimum sea ice extents can be affected by sea ice-
770 ocean exchanges, sea ice processes, and ice dynamics. We also demonstrated quantitatively how
771 atmospheric feedback can enhance the effect of perturbations, but also in some cases dampen it.
772 Although it is an idealized study, it highlights the major role of albedo and sea ice transport in the sea
773 ice extent seasonal cycle and as key processes to target in model development and process
774 understanding.

775 **Code and data availability**

776 As described in detail in Pelletier et al. (2022a), the PARASO sources can be obtained by CLM-
777 Community members on their RedC (<https://redc.clm-community.eu/> then “COSMO-CLM” then
778 “Downloads”). All PARASO sources, except the COSMO routines, are publicly available for didactic
779 purposes at <https://doi.org/10.5281/zenodo.5576201> (Pelletier et al., 2021) as well as the files to run
780 the model in the same configuration as here (Pelletier and Helsen, 2021). The NEMO3.6 version is
781 available from <https://forge.ipsl.jussieu.fr/nemo/browser/branches/UKMO> (Mathiot and Storkey,
782 2018).

783 **Supplement link:**

784 Supplementary information is available as a separate file.

785 **Author contributions.** HG initiated the study and designed the sensitivity experiments after
786 discussions with all the co-authors. FK performed the simulations. FK and PVH prepared the model
787 outputs for the analyses. HG made the analyses and the figures and all the co-authors contribute in
788 the interpretation of the results. HG wrote the manuscript, with inputs from all co-authors

789 **Competing interests:**

790 The authors declare that they have no conflict of interest.

791 **Acknowledgements.** This work was performed in the framework of the PARAMOUR project,
792 “Decadal predictability and variability of polar climate: the role of atmosphere-ocean-cryosphere
793 multiscale interactions”, supported by the Fonds de la Recherche Scientifique – FNRS and the FWO
794 under the Excellence of Science (EOS) program (grant no. 00100718F, EOS ID no. 30454083). The

795 computational resources were provided by the VSC (Flemish Supercomputer Center), funded by the
796 Research Foundation Flanders (FWO) and the Flemish Government, the Center for High Performance
797 Computing and Mass Storage (CISM) of the Université catholique de Louvain (CISM/UCL) and the
798 Consortium des Équipements de Calcul Intensif en Fédération Wallonie Bruxelles (CÉCI), funded by the
799 Fond de la Recherche Scientifique de Belgique (F.R.S.-FNRS) under convention 2.5020.11 and by the
800 Walloon region. HG is research director with the F.R.S.-FNRS. EBW was supported by the Office of
801 Naval Research-DRI grant N00014-18-1-2175. LR was supported by the National Oceanic and
802 Atmospheric Administration (NOAA) Climate and Global Change Postdoctoral Fellowship Program,
803 which is administered by UCAR's Cooperative Programs for the Advancement of Earth System Science
804 (CPAESS) under award NA18NWS4620043B.

805

806 **References**

807 Alberello, A., Bennetts, L., Heil, P., Eayrs, C., Vichi, M., MacHutchon, K., Onorato, M., and Toffoli,
808 A.: Drift of pancake ice floes in the winter antarctic marginal ice zone during polar cyclones, *J.*
809 *Geophys. Res.—Oceans* 125, e2019JC015418, 2020.

810 Barthélemy, A., Fichet, T., Goosse, H., and Madec, G.: Modelling the interplay between sea ice
811 formation and the oceanic mixed layer: limitations of simple brine rejection parameterizations.
812 *Ocean Modelling* 86, 141-152, 2015.

813 Bitz, C. M. and Lipscomb, W. H.: An energy-conserving thermodynamic model of sea ice, *J.*
814 *Geophys. Res.—Oceans*, 104, 15669– 15677, <https://doi.org/10.1029/1999JC900100>, 1999.

815 Bitz, C. M., Holland, M. M., Weaver, A. J., and Eby, M.: Simulating the ice-thickness distribution
816 in a coupled climate model, *J. Geophys. Res.—Oceans*, 106, 2441–2463,
817 <https://doi.org/10.1029/1999JC000113>, 2001.

818 Bitz, C. M. and Roe, G. H.: A mechanism for the high rate of sea ice thinning in the Arctic Ocean,
819 *J. Clim.* 17, 3623–3632, 2004.

820 Bouillon, S., Fichet, T., Legat, V., and Madec, G.: The elastic– viscous–plastic method revisited,
821 *Ocean Model.*, 71, 2–12, <https://doi.org/10.1016/j.ocemod.2013.05.013>, 2013.

822 Brandt, R. E., Warren, S. G., Worby, A. P., and Grenfell, T. C.: Surface Albedo of the Antarctic Sea
823 Ice Zone, *J. Climate*, 18, 3606– 3622, <https://doi.org/10.1175/JCLI3489.1>, 2005.

824 Chevallier, M., Massonnet, F., Goessling, H., Guémas, V., and Jung, T. : The Role of Sea Ice in Sub-
825 seasonal Predictability, In *Sub-Seasonal to Seasonal Prediction*, 201–221, Elsevier.
826 <https://doi.org/10.1016/B978-0-12-811714-9.00010-3>, 2019.

827 Doms, G., Förstner, J., Heise, E., Herzog, H.-J., Mironov, D., Raschendorfer, M., Renhardt, T.,
828 Ritter, B., Schrodin, R., Schulz, J.-P., and Vogel, G.: COSMO-Model Version 5.05: A Description of the
829 Nonhydrostatic Regional COSMO-Model – Part I: Dynamics and Numerics, Tech. rep., Consortium for
830 Small-Scale Modelling, https://doi.org/10.5676/DWD_PUB/NWV/COSMODOC_5.05_II, 2018.

831 Downes, S.M., Farneti, R., Uotila, P., Griffies, S.M., Marsland, S.J., Bailey, D., Behrens, E.,
832 Bentsen, M., Bi, D., Biastoch, A., Böning, C., Bozec, A., Canuto, V.M., Chassignet, E., Danabasoglu, G.,
833 Danilov, S., Diansky, N., Drange, H., Fogli, P.G., Gusev, A., Howard, A., Ilicak, M., Jung, T., Kelley, M.,
834 Large, W.G., Leboissetier, A., Long, M., Jianhua, L., Masina, S., Mishra, A., Antonio Navarra, A.J.,
835 Nurser, G., Patara, L., Samuels, B.L., Sidorenko, D., Spence, P., Tsujino, H., Wang, Q., and Yeager, S.G.:
836 An assessment of southern ocean water masses and sea ice during 1988–2007 in a suite of
837 interannual core-ii simulations, *Ocean. Modell.* 94:67–94. <https://doi.org/10.1016/j.ocemod.2015.07.022>, 2015.

838 ://doi.org/10.1016/j.ocemod.2015.07.022, 2015.

839 Eayrs, C., Holland, D. M., Francis, D., Wagner, T. J. W., Kumar, R., and Li, X.: Understanding the
840 seasonal cycle of Antarctic sea ice extent in the context of longer-term variability, *Rev. Geophys.*, 57,
841 <https://doi.org/10.1029/2018RG000631>, 2019.

842 Eayrs, C., Faller, D., and Holland, D.M.: Mechanisms driving the asymmetric seasonal cycle of
843 Antarctic Sea Ice in the CESM Large Ensemble, *Ann. Glac.* 1–10. <https://doi.org/10.1017/aog.2020.26>,
844 2020

845 Enomoto, H., and Ohmura, A.: The influences of atmospheric half-yearly cycle on the sea ice
846 extent in the Antarctic, *J. Geophys. Res.* 95, 9497, 1990.

847 Fetterer, F., Knowles, K., Meier, W. N., Savoie, M., and Windnagel, A. K.: Sea Ice Index, Version 3
848 [Data Set]. Boulder, Colorado USA. National Snow and Ice Data Center.
849 <https://nsidc.org/data/g02135/versions/3>, 2017.

850 Fichet, T., and Morales Maqueda, M.A. : Sensitivity of a global sea ice model to the treatment
851 of ice thermodynamics and dynamics, *J. Geophys. Res.*, 102(C6), 12,609–12,646, 1997.

Code de champ modifié

Code de champ modifié

Code de champ modifié

Code de champ modifié

852 Gaspar, P., Grégoris, Y., and Lefevre, J.-M.: A simple eddy kinetic energy model for simulations of
853 the oceanic vertical mixing: Tests at station Papa and long-term upper ocean study site, *J. Geophys.*
854 *Res.-Oceans*, 95, 16179–16193, <https://doi.org/10.1029/JC095iC09p16179>, 1990.

855 Goosse, H., Kay, J. E., Armour, K., Bodas-Salcedo, A., Chepfer, H., Docquier, D., Jonko, A.,
856 Kushner, P. J., Lecomte, O., Massonnet, F., Park, H.-S., Pithan, F., Svensson, G., Vancoppenolle, M.:
857 Quantifying climate feedbacks in polar regions, *Nat. Comm.* 9, 1919, DOI: 10.1038/s41467-018-
858 04173-0, 2018.

859 Gordon, A. L.: Seasonality of Southern Ocean sea ice, *J. Geophys. Res.* 86, 4193–284, 1981.

860 Grenfell, T. C. and Perovich, D. K.: Seasonal and spatial evolution of albedo in a snow-ice-land-
861 ocean environment, *J. Geophys. Res.-Oceans*, 109, 8044, <https://doi.org/10.1029/2003JC001866>,
862 2004.

863 Handcock, M.S., and Raphael, M. N.: Modeling the annual cycle of daily Antarctic sea ice extent.
864 *The Cryosphere*, 14, 2159–2172, 2020, <https://doi.org/10.5194/tc-14-2159-2020>, 2020.

865 Hersbach, H., Bell, B., Berrisford, P., Hirahara, S., Horányi, A., Muñoz-Sabater, J., Nicolas, J.,
866 Peubey, C., Radu, R., Schepers, D., Simmons, A., Soci, C., Abdalla, S., Abellan, X., Balsamo, G.,
867 Bechtold, P., Biavati, G., Bidlot, J., Bonavita, M., De Chiara, G., Dahlgren, P., Dee, D., Diamantakis, M.,
868 Dragani, R., Flemming, J., Forbes, R., Fuentes, M., Geer, A., Haimberger, L., Healy, S., Hogan, R. J.,
869 Hólm, E., Janisková, M., Keeley, S., Laloyaux, P., Lopez, P., Lupu, C., Radnoti, G., de Rosnay, P., Rozum,
870 I., Vamborg, F., Villaume, S., and Thépaut, J.-N.: The ERA5 global reanalysis, *Q. J. Roy. Meteor. Soc.*,
871 146, 1999–2049, <https://doi.org/10.1002/qj.3803>, 2020.

872 Hobbs, W. R., Massom, R., Stammerjohn, S., Reid, P., Williams, G., and Meier, W.: A review of
873 recent changes in Southern Ocean sea ice, their drivers and forcings, *Global and Planetary Change*,
874 143, 228–250, 10.1016/j.gloplacha.2016.06.008, 2016.

875 [Holland, P.R., Kwok R.: Wind-driven trends in Antarctic sea-ice drift. *Nat Geosci* 5, 872–875. doi:10.1038/ngeo1627, 2012.](https://doi.org/10.1038/ngeo1627)

876 [Holland, P. R., The seasonality of Antarctic sea ice trends, *Geophys. Res. Lett.*, 41, 4230–4237. doi:10.1002/2014GL060172, 2014.](https://doi.org/10.1002/2014GL060172)

877 [Holland, P.R., and Kimura, N.: Observed Concentration Budgets of Arctic and Antarctic Sea Ice, *J. Clim.*, 29 5241–6249, 2016.](https://doi.org/10.1002/2014GL060172)

878 [Horvat, C: Marginal ice zone fraction benchmarks sea ice and climate model skill, *Nat. Commun.* 12, 2221, https://doi.org/10.1038/s41467-021-22004-7, 2021.](https://doi.org/10.1038/s41467-021-22004-7)

879 [Kacimi, S., and Kwok, R.: The Antarctic sea ice cover from ICESat-2 and CryoSat-2: freeboard, snow depth, and ice thickness. *The Cryosphere* 14, 4453–4474, 10.5194/tc-14-4453-2020, 2020.](https://doi.org/10.1038/s41467-021-22004-7)

880 [Kusahara, K., Williams, G., Massom, R., Reid, P., and Hasumi, H.: Spatiotemporal dependence of Antarctic sea ice variability to dynamic and thermodynamic forcing: A coupled ocean–sea ice model study, *Clim. Dynam.*, 52, 3791–3807, https://doi.org/10.1007/s00382-018-4348-3, 2019.](https://doi.org/10.1007/s00382-018-4348-3)

881 [Large, W. G., and Yeager, S. G: Diurnal to decadal global forcing for ocean and sea-ice models: The data sets and flux climatologies, *Tech. Rep.*, National Center for Atmospheric Research., https://doi.org/10.5065/D6KK98Q6, 2004.](https://doi.org/10.5065/D6KK98Q6)

882 [Lazar, A., Madec, G., and Delecluse, P.: The deep interior downwelling, the Veronis effect, and mesoscale tracer transport parameterizations in an OGCM, *J. Phys. Oceanogr.*, 29, 2945–2961. https://doi.org/10.1175/1520-0485\(1999\)029%3C2945:TDIDTV%3E2.0.CO;2, 1999.](https://doi.org/10.1175/1520-0485(1999)029%3C2945:TDIDTV%3E2.0.CO;2)

883 [Lecomte, O., Goosse, H., Fichet, T., Holland, P. R., Uotila, P., Zunz, V., Kimura, N.: Impact of surface wind biases on the Antarctic sea ice concentration budget in climate models. *Ocean Modelling* 105, 60–70. https://doi.org/10.1016/j.ocemod.2016.08.001, 2016.](https://doi.org/10.1016/j.ocemod.2016.08.001)

884 [Madec, G., Bourdallé-Badie, R., Bouttier, P.-A., Bricaud, C., Bruciaferri, D., Calvert, D., Chanut, J., Clementi, E., Coward, A., Delrosso, D., Ethé, C., Flavoni, S., Graham, T., Harle, J., Iovino, D., Lea, D., Lévy, C., Lovato, T., Martin, N., Masson, S., Mocavero, S., Paul, J., Rousset, C., Storkey, D., Storto, A.,](https://doi.org/10.1016/j.ocemod.2016.08.001)

Code de champ modifié

Code de champ modifié

Code de champ modifié

Code de champ modifié

900 and Vancoppenolle, M.: NEMO ocean engine, Tech. rep., Insitut Pierre-Simon Laplace, Zenodo [code],
901 <https://doi.org/10.5281/zenodo.3248739>, 2017.

902 Marchi, S., Fichefet, T., Goosse, H.: influence of the initial ocean state on the predictability of the
903 Antarctic sea ice at the seasonal timescale: a study with NEMO3.6-LIM3. *Ocean Modelling* 148,
904 101591, <https://doi.org/10.1016/j.ocemod.2020.101591>, 2020.

905 Martinson, D. G.: Evolution of the Southern Ocean winter mixed layer and sea ice-open ocean
906 deep-water formation and ventilation, *J. Geophys. Res. Oceans* 95, 11641–11654, 1990.

907 Massom, R., Reid, P., Stammerjohn, S., Raymond, B., Fraser, A., Ushio, S.: Change and variability
908 in East Antarctic sea ice seasonality, 1979/80–2009/10. *PLoS ONE*. <https://doi.org/10.1371/journal.pone.0064756>, 2013.

909
910 Massonnet, F., Vancoppenolle, M., Goosse, H., Docquier, D., Fichefet, T., Blanchard-
911 Wrigglesworth, E., and Bitz, C. M.: Arctic sea-ice variability tied to its mean state through
912 thermodynamic feedbacks. *Nature Climate Change*, 8, 599–603, [10.1038/s41558-018-0204-z](https://doi.org/10.1038/s41558-018-0204-z), 2018.

913 Massonnet, F., Barthélemy, A., Worou, K., Fichefet, T., Vancoppenolle, M., Rousset, C., and
914 Moreno-Chamarro, E.: On the discretization of the ice thickness distribution in the NEMO3.6-LIM3
915 global ocean–sea ice model, *Geosci. Model Dev.*, 12, 3745–3758, <https://doi.org/10.5194/gmd-12-3745-2019>, 2019.

916
917 Mathiot, P., Jenkins, A., Harris, C., and Madec, G.: Explicit representation and parametrised
918 impacts of under ice shelf seas in the z - coordinate ocean model NEMO 3.6, *Geosci. Model Dev.*, 10,
919 2849–2874, <https://doi.org/10.5194/gmd-10-2849-2017>, 2017.

920 Mathiot, P. and Storkey, D.: NEMO model code, MetOffice (UK) branch
921 dev_isf_remapping_UKESM_GO6package_r9314, revision 11248, MetOffice [code], available at:
922 [https://forge.ipsl.jussieu.fr/nemo/browser/branches/UKMO/dev_isf_remapping_UKESM_GO6packa](https://forge.ipsl.jussieu.fr/nemo/browser/branches/UKMO/dev_isf_remapping_UKESM_GO6package_r9314?rev=15667)
923 [ge_r9314?rev=15667](https://forge.ipsl.jussieu.fr/nemo/browser/branches/UKMO/dev_isf_remapping_UKESM_GO6package_r9314?rev=15667) (last access 21 January 2022), 2018.

924 Maykut, G. A. The surface heat and mass balance. *The Geophysics of Sea Ice* (ed. Untersteiner,
925 N.), Plenum Press, 395–464, 1986.

926 Nie, Y., Uotila, P., Cheng, B., Massonnet, F., Kimura, N., Cipollone, A., Lv, X. : Southern Ocean sea
927 ice concentration budgets of five ocean-sea ice reanalyses, *Clim. Dyn.* [https://doi.org/10.1007/s00382-](https://doi.org/10.1007/s00382-022-06260-x)
928 [022-06260-x](https://doi.org/10.1007/s00382-022-06260-x), 2022.

929 Nihashi, S., and Cavalieri, D. J.: Observational evidence of a hemispheric-wide ice–ocean albedo
930 feedback effect on Antarctic sea-ice decay. *Journal of Geophysical Research*, 111, C12001.
931 <https://doi.org/10.1029/2005JC003447>, 2006.

932 Oleson, K. W., Lawrence, D. M., Bonan, G. B., Drewniak, B., Huang, M., Koven, C. D., Levis, S., Li,
933 F., Riley, W. J., Subin, Z. M., Swenson, S. C., Thornton, P. E., Bozbiyik, A., Fisher, R., Heald, C. L.,
934 Kluzek, E., Lamarque, J.-F., Lawrence, P. J., Leung, L. R., Lipscomb, W., Muszala, S., Ricciuto, D. M.,
935 Sacks, W., Sun, Y., Tang, J., and Yang, Z.-L.: Technical Description of version 4.5 of the Community
936 Land Model (CLM), Tech. Rep. July, NCAR, available at:
937 http://www.cesm.ucar.edu/models/cesm1.2/clm/CLM45_Tech_Note.pdf (last access: 21 January
938 2022), 2013.

939 Parkinson, C.L.: Global Sea Ice Coverage from Satellite Data: Annual Cycle and 35-Yr Trends. *J.*
940 *Clim.* 27, 9377–9382, 2014.

941 Parkinson, C. L.: A 40-y record reveals gradual Antarctic sea ice increases followed by decreases
942 at rates far exceeding the rates seen in the Arctic, *Proc. Nat. Acad. Sciences* 116, 14414–14423,
943 [10.1073/pnas.1906556116](https://doi.org/10.1073/pnas.1906556116), 2019.

944 Pelletier, C. and Helsen, S.: PARASO ERA5 forcings, Zenodo [dataset],
945 <https://doi.org/10.5281/zenodo.5590053>, 2021.

Code de champ modifié

Code de champ modifié

Code de champ modifié

946 Pelletier C., Klein, F., Zipf, L., Haubner, K., Mathiot, P., Pattyn, F., Moravveji, E., and Vanden
947 Broucke, S.: PARASO source code (no COSMO), Zenodo [code],
948 <https://doi.org/10.5281/zenodo.5576201>, 2021.

949 Pelletier C., Fichefet, T., Goosse, H., Haubner, K., Helsen, S., Huot, P.-V., Kittel, C., Klein, F., Le
950 clec'h, S., van Lipzig, N. P. M., Marchi, S., Massonnet, F., Mathiot, P., Moravveji, E., Moreno, E.,
951 Ortega, P., Pattyn, F., Souverijns, N., Van Achter, G., Vanden Broucke, S., Vanhulle, A., Verfaillie, D.,
952 and Zipf, L.: PARASO, a circum-Antarctic fully-coupled ice-sheet - ocean - sea-ice - atmosphere - land
953 model involving f.ETISH1.7, NEMO3.6, LIM3.6, COSMO5.0 and CLM4.5 Geosci. Model Dev. 15, 553–
954 594, <https://doi.org/10.5194/gmd-15-553-2022>, 2022a.

955 Pelletier C., Fichefet, T., Goosse, H., Haubner, K., Helsen, S., Huot, P.-V., Kittel, C., Klein, F., Le
956 clec'h, S., van Lipzig, N. P. M., Marchi, S., Massonnet, F., Mathiot, P., Moravveji, E., Moreno, E.,
957 Ortega, P., Pattyn, F., Souverijns, N., Van Achter, G., Vanden Broucke, S., Vanhulle, A., Verfaillie, D.,
958 and Zipf, L.: Corrigendum to 'PARASO, a circum-Antarctic fully-coupled ice-sheet - ocean - sea-ice -
959 atmosphere - land model involving f.ETISH1.7, NEMO3.6, LIM3.6, COSMO5.0 and CLM4.5' Corr. to
960 Geosci. Model Dev. 15, 553–594, <https://doi.org/10.5194/gmd-15-553-2022-corrigendum>; 2022b.

961 Raphael, M. N., Handcock, M. S., Holland, M. M. and Landrum, L. L.: An assessment of the
962 temporal variability in the annual cycle of daily Antarctic sea ice in the NCAR Community Earth
963 System Model, Version 2: A comparison of the historical runs with observations, J. Geophys. Res.:
964 Oceans 125, e2020JC01645, <https://doi.org/10.1029/2020JC016459>, 2020.

965 Roach, L. A., Horvat, C., Dean, S. M., and Bitz, C. M.: An emergent sea ice floe size distribution in
966 a global coupled ocean-sea ice model, J. Geophys. Res.: Oceans, 123, 4322–4337,
967 <https://doi.org/10.1029/2017JC013692>, 2018.

968 Roach, L. A., Bitz, C. M., Horvat, C., and Dean, S. M.: Advances in modeling interactions between
969 sea ice and ocean surface waves. J. Adv. Mod. Earth Sys. 11, 4167–4181,
970 <https://doi.org/10.1029/2019MS001836>, 2019.

971 Roach, L. A., Dörr, J., Holmes, C. R., Massonnet, F., Blockley, E.W., Notz, D., Rackow, T., Raphael,
972 M. N., O'Farrell, S. P., Bailey, D. A., Bitz, C. M.: Antarctic sea ice area in CMIP6, Geophys. Res. Lett., 47,
973 e2019GL086729, <https://doi.org/10.1029/2019GL086729>, 2020.

974 Roach, L.A., Eisenman, I., Wagner, T. J. W., Blanchard-Wrigglesworth, E., Bitz, C. M.: Asymmetry
975 in the seasonal cycle of Antarctic sea ice due to Insolation. Nat. Geosci. 15, 277–281,
976 <https://doi.org/10.1038/s41561-022-00913-6>, 2022.

977 Rockel, B., Will, A., and Hense, A.: The regional climate model COSMO-CLM (CCLM), Meteorol.
978 Z., 17, 347–348, <https://doi.org/10.1127/0941-2948/2008/0309>, 2008.

979 Rousset, C., Vancoppenolle, M., Madec, G., Fichefet, T., Flavoni, S., Barthélemy, A., Benshila, R.,
980 Chanut, J., Levy, C., Masson, S., and Vivier, F.: The Louvain-La-Neuve sea ice model LIM3.6: global and
981 regional capabilities, Geosci. Model Dev., 8, 2991–3005, <https://doi.org/10.5194/gmd-8-2991-2015>,
982 2015.

983 Schroeter, S., and Sandery, P.A.: Large-ensemble analysis of Antarctic sea ice model sensitivity to
984 parameter uncertainty, Ocean Modelling 177, 102090,
985 <https://doi.org/10.1016/j.ocemod.2022.102090>, 2022.

986 Souverijns, N., Gossart, A., Gorodetskaya, I. V., Lhermitte, S., Mangold, A., Laffineur, Q., Delcloc,
987 A., and van Lipzig, N. P. M.: How does the ice sheet surface mass balance relate to snowfall? Insights
988 from a ground-based precipitation radar in East Antarctica, The Cryosphere, 12, 1987–2003,
989 <https://doi.org/10.5194/tc-12-1987-2018>, 2018.

990 Stammerjohn, S.E., Martinson, D.G., Smith, R.C., Yuan, X., and Rind, D.: Trends in Antarctic
991 annual sea ice retreat and advance and their relation to El Niño–Southern Oscillation and Southern
992 Annular Mode variability. J Geophys Res 113:1–20. <https://doi.org/10.1029/2007JC004269>, 2008.

Code de champ modifié

Code de champ modifié

Code de champ modifié

Code de champ modifié

Code de champ modifié

Code de champ modifié

Code de champ modifié

Code de champ modifié

993 Stewart, K., Kim, M., Urakawa, S., McC.Hogg, A., Yeager, S., Tsujino, H., Nakano, H., Kiss, A.E.,
994 Danabasoglu, G.: JRA55-do-based repeat year forcing datasets for driving ocean–sea-ice models,
995 Ocean Model. 147, 101557, <https://doi.org/10.1016/j.ocemod.2019.101557>, 2020.

996 [Sun S., Eisenman I.: Observed Antarctic sea ice expansion reproduced in a climate model after](https://doi.org/10.1038/s41467-021-21412-z)
997 [correcting biases in sea icedrift velocity. Nature Communications 12,1060,](https://doi.org/10.1038/s41467-021-21412-z)
998 <https://doi.org/10.1038/s41467-021-21412-z>, 2021.

999 Urrego-Blanco, J. R., Urban, N. M., Hunke, E. C., Turner, A. K., and Jeffery, N.: Uncertainty
1000 quantification and global sensitivity analysis of the Los Alamos sea ice model, J. Geophys. Res. Oceans
1001 121, 2709–2732, doi:10.1002/2015JC011558, 2016.

1002 Vancoppenolle, M., Fichefet, T., Goosse, H., Bouillon, S., Madec, G., and Maqueda, M. A. M.:
1003 Simulating the mass balance and salinity of Arctic and Antarctic sea ice. 1. Model description and
1004 validation, Ocean Model., 27, 33–53, <https://doi.org/10.1016/j.ocemod.2008.10.005>, 2009.

1005 Vancoppenolle, M., Bouillon, S., Fichefet, T., Goosse, H. Lecomte, O., Morales Maqueda, M. A.,
1006 and Madec, G.: LIM The Louvain-la-Neuve sea Ice Model, Tech. Rep. 31, Note du Pôle de
1007 Modélisation de l’Institut Pierre-Simon Laplace No. 31, ISSN No 1288-1619, available at:
1008 https://cmc.ipsl.fr/images/publications/scientific_notes/lim3_book.pdf (last access 21 July 2022),
1009 2012.

1010 Verfaillie, D., Pelletier, C., Goosse, H., Jourdain, N.C., Bull, C.Y.S., Dalaiden, Q., Favier, V.,
1011 Fichefet, T., and Wille, J. : How does the Southern Annular Mode impact ice-shelf basal melt in
1012 Antarctica? Comm. Earth Envi. 3, 139, <https://doi.org/10.1038/s43247-022-00458-x>, 2022.

1013 Watkins, A. B., and Simmonds, I.: A late spring surge in the open water of the Antarctic sea ice
1014 pack, Geophys. Res. Lett., 26, 1481–1484. <https://doi.org/10.1029/1999GL900292>, 1999

1015 Wilson, E.A., Riser, S. C., Campbell, E. C., and Wong, A. P.: Winter upper ocean stability and ice-
1016 ocean feedbacks in the sea-ice-covered Southern Ocean. Journal of Physical Oceanography, 49,
1017 1099–1117, 2019.

1018 Zuo, H., Balmaseda, M. A., Tietsche, S., Mogensen, K., and Mayer, M: The ECMWF operational
1019 ensemble reanalysis–analysis system for ocean and sea ice: a description of the system and
1020 assessment, Ocean Sci. 15, 779–808, <https://doi.org/10.5194/os-15-779-2019>, 2019.

Code de champ modifié

Code de champ modifié

Code de champ modifié

Code de champ modifié

1022 **Supplementary Material**

1023 **Modulation of the seasonal cycle of the Antarctic sea ice extent by sea ice**
1024 **processes and feedbacks with the ocean and the atmosphere**

1025

1026 Hugues Goosse¹, Sofia Allende Contador¹, Cecilia M. Bitz², Edward Blanchard-Wrigglesworth², Clare
1027 Eayrs³, Thierry Fichefet¹, Kenza Himmich⁴, Pierre-Vincent Huot⁵, François Klein¹, Sylvain Marchi⁵,
1028 François Massonnet¹, Bianca Mezzina¹, Charles Pelletier⁶, Lettie Roach^{7,8}, Martin Vancoppenolle⁴,
1029 Nicole P.M. van Lipzig⁵

1030 1. Earth and Life Institute, Université catholique de Louvain, Belgium

1031 2. Department of Atmospheric Sciences, University of Washington, Seattle, USA

1032 ~~3.~~ [3. Korea Polar Research Institute, Incheon, South Korea](#)

1033 ~~3-4.~~ [3-4. Sorbonne Université, Laboratoire d'Océanographie et du Climat \(LOCEAN-IPSL\), CNRS, IRD,](#)
1034 [MNHN, Paris, France](#)

1035 ~~4-5.~~ [4-5. Department of Earth and Environmental Sciences, KU Leuven, Leuven, Belgium](#)

1036 ~~5-6.~~ [5-6. European Centre for Medium-Range Weather Forecasts, Bonn, Germany](#)

1037 ~~6-7.~~ [6-7. NASA Goddard Institute for Space Studies, New York, NY, USA](#)

1038 ~~7-8.~~ [7-8. Center for Climate Systems Research, Columbia University, New York, NY, USA](#)

1039

1040

1041

1042 Corresponding author: Hugues Goosse hugues.goose@uclouvain.be

1043

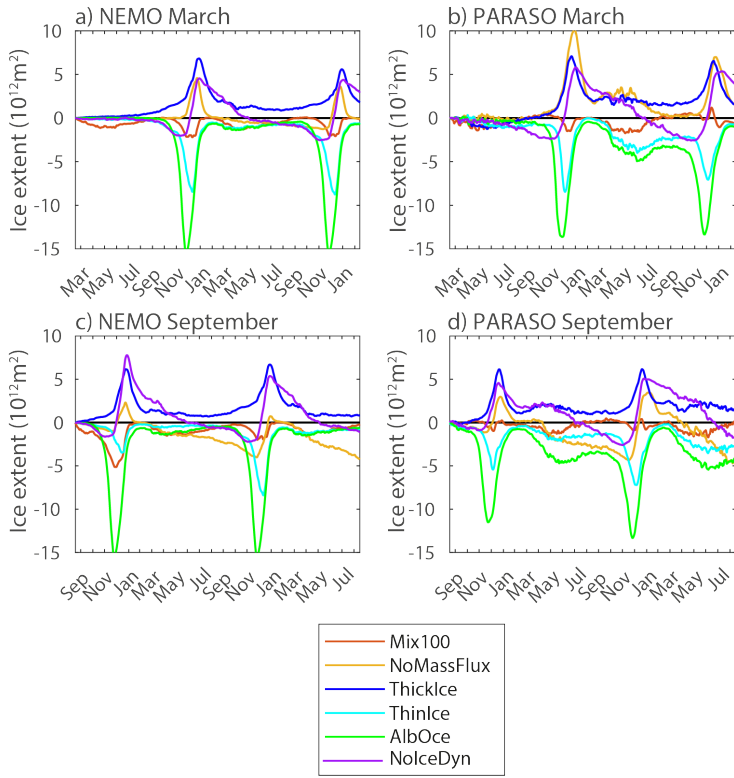
1044 [Submitted in revised form to The Cryosphere 5-01-2023.](#)

1045

1046 Supplementary discussion: temperature response in ThickIce and ThinIce experiments
1047 In ThickIce, a cooling is observed in summer and in regions in winter close to the ice edge compared
1048 to the reference experiment (Fig. S5) due to the larger sea ice extent. However, this does not
1049 overwhelm the effect of the larger winter sea ice formation (Fig. 4) and thus the larger heat fluxes to
1050 the atmosphere within the pack that leads to an air temperature increase that dominates the regional
1051 mean (Fig. 8).

1052 The opposite should occur in the ThinIce experiments. The lower sea ice formation (Fig. 4) and oceanic
1053 heat losses in ThinIce should lead to a cooling of the atmosphere within the ice pack, while the smaller
1054 ice extent should be associated with an atmospheric warming in the regions that are ice free in ThinIce
1055 and ice covered in the reference experiment. However, we find that the atmospheric warming due to
1056 a reduced ice extent expands to most of the pack in ThinIce, even in winter with cooling restricted to
1057 some regions close to the continent (Fig. S5). This extended warming is likely due to the strong changes
1058 in albedo and absorbed solar radiation in ThinIce (Fig. S4). The dominant role of the albedo is consistent
1059 with the generally colder temperatures in the first winter of ThinIce PARA Mar (Fig. 8), when the
1060 albedo effect did not yet have the time to act given that the experiments start at the end of summer.
1061 The larger fraction of leads within the ice pack also contributes to the warming in ThinIce.

1063

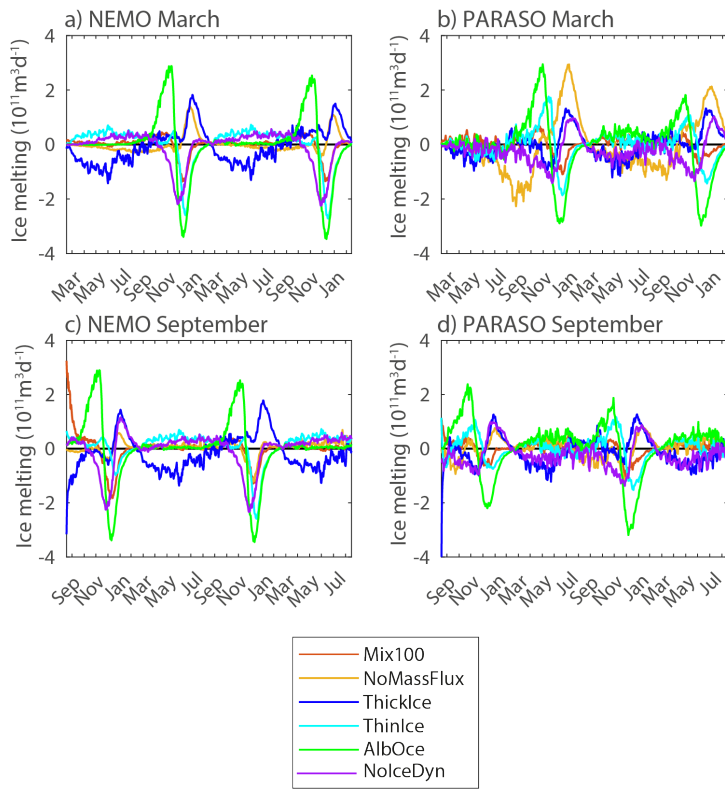


1064

1065 Figure S1. Anomaly of Antarctic sea ice extent (in 10¹² m²) compared to the corresponding reference
1066 simulation in the group of experiments starting in March (top row) and September (bottom) for the
1067 NEMO (left column) and PARASO configurations (right column).

1068

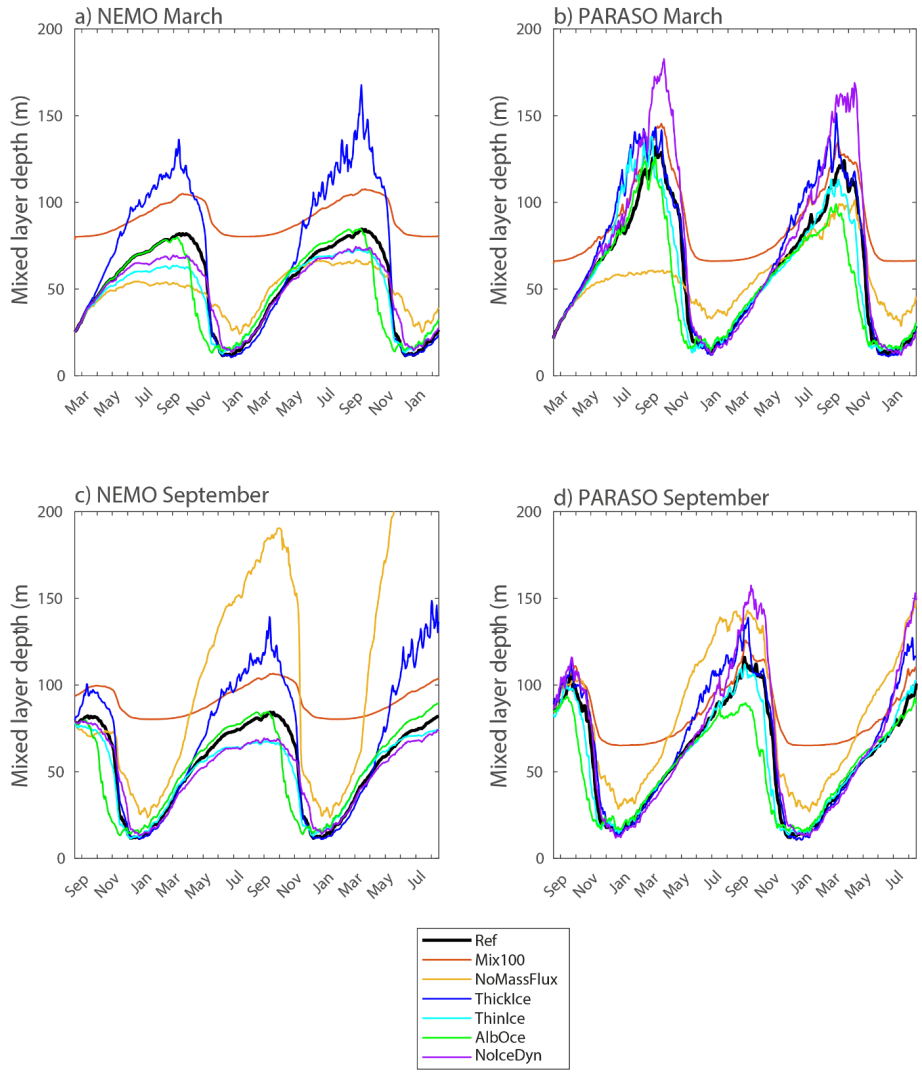
1069



1070

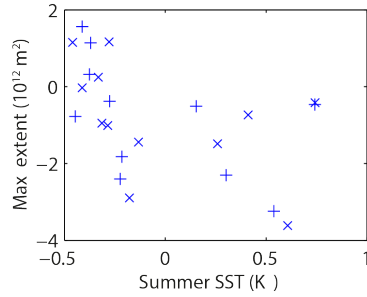
1071 Figure S2. Anomaly of mass flux due to sea ice growth and melt (counted positive for melting)
 1072 integrated over the Southern Ocean (in $10^{11} \text{m}^3 \text{d}^{-1}$) compared to the corresponding reference
 1073 simulation in the group of experiments starting in March (top row) and September (bottom) for the
 1074 NEMO (left column) and PARASO configurations (right column).

1075

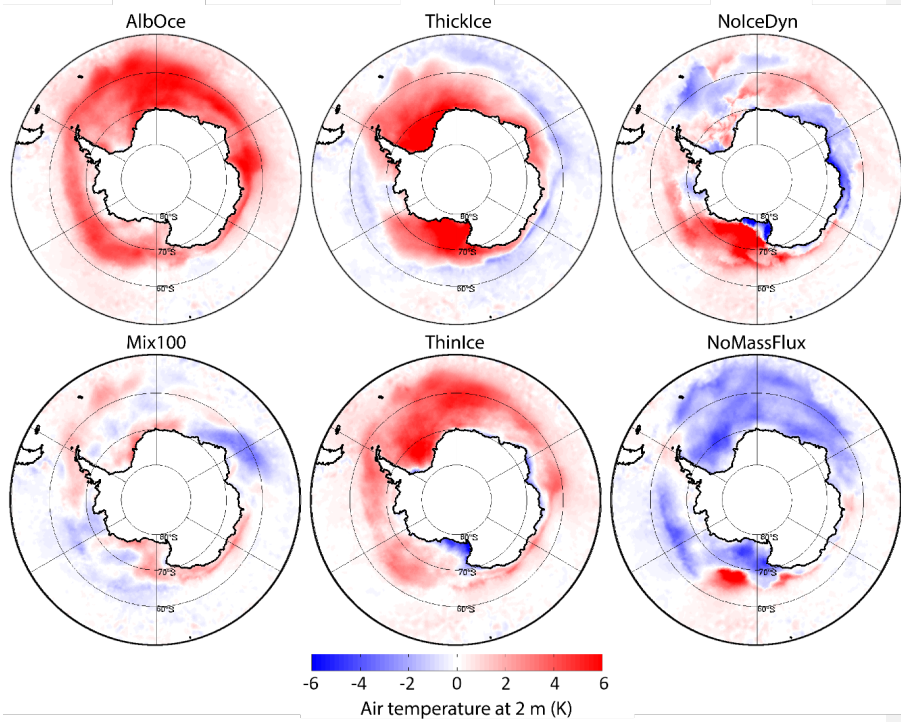


1076
 1077 **Figure S3.** Mixed layer depth (in m) averaged over the ocean region south of 60°S in the group of
 1078 experiments starting in March (top row) and September (bottom) for the NEMO (left column) and
 1079 PARASO configurations (right column).

1080

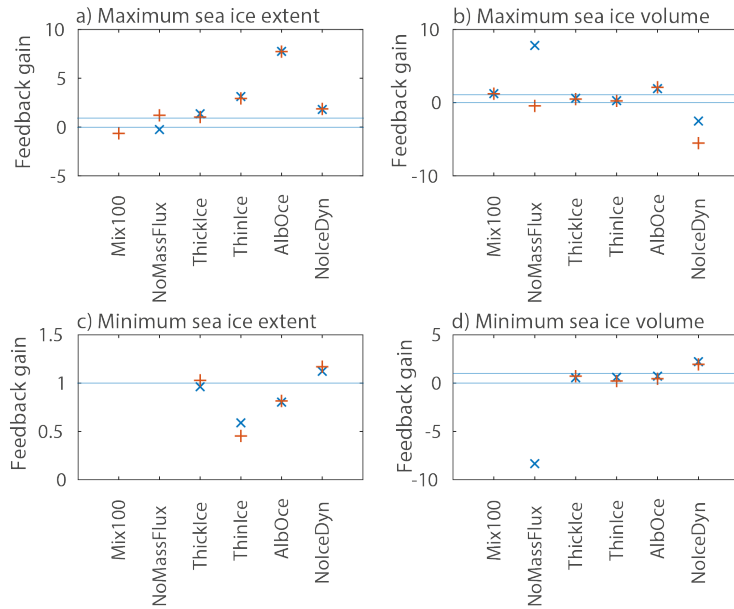


1081
 1082 **Figure S4.** Maximum sea ice extent anomaly (in 10^{12}m^2) compared to the reference experiment as a
 1083 function of the sea surface anomaly averaged over the region south of 60°S (in K) in the previous
 1084 summer for the second year in the experiments starting in March and for the first minimum and second
 1085 maximum for the experiments starting in September.



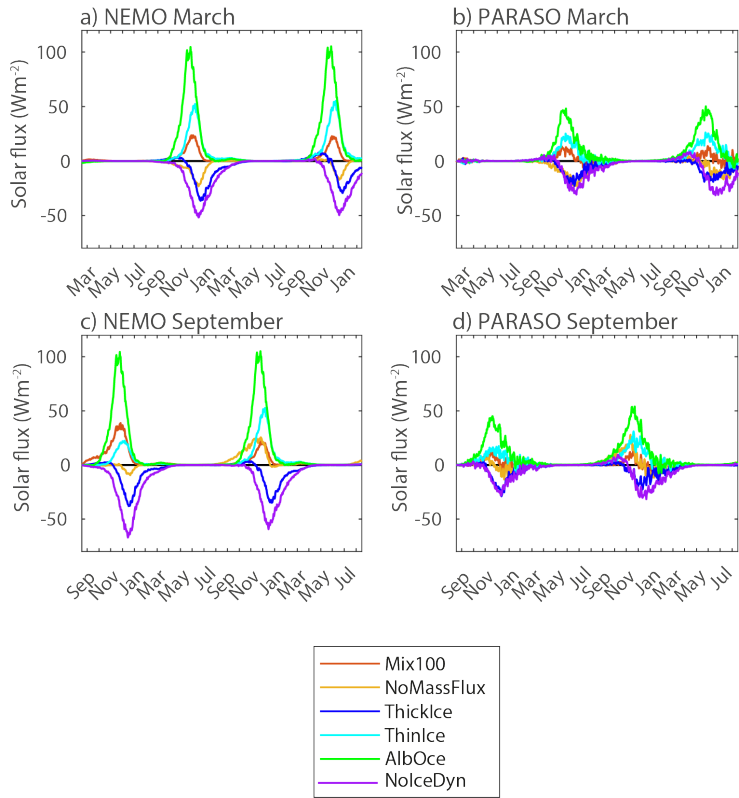
1086
 1087 **Figure S5.** Difference in surface air temperature (in K) between the PARASO experiment in winter (July-
 1088 August-September) of the second year of the experiment starting in March and the corresponding
 1089 reference experiment.

1090



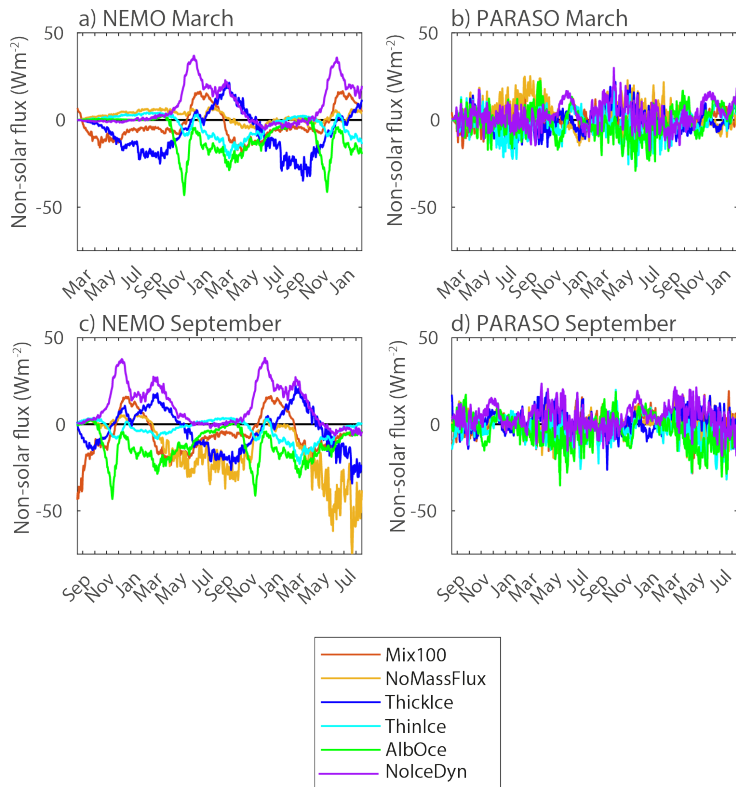
1091
 1092 **Figure S6.** Feedback gain for experiments starting in March (blue x) and September (red +) for the a)
 1093 maximum sea ice extent, b) maximum sea ice volume, c) minimum sea ice extent and d) minimum sea
 1094 ice volume. We have not displayed the feedback gain when the uncoupled response is smaller than
 1095 0.2 million km² for sea ice extent or 0.2 thousand km³ for sea ice volume to avoid large numbers of the
 1096 feedback gains, as this value is used in the denominator of G . Light blue lines are drawn at values of 0
 1097 and 1.

1098



1099

1100 **Figure S7. Anomaly of net solar** radiation at the top of the ocean (in W m^{-2}) averaged over the ocean
 1101 region south of 60°S compared to the corresponding reference simulation in the group of experiments
 1102 starting in March (top row) and September (bottom) for the NEMO (left column) and PARASO
 1103 configurations (right column).

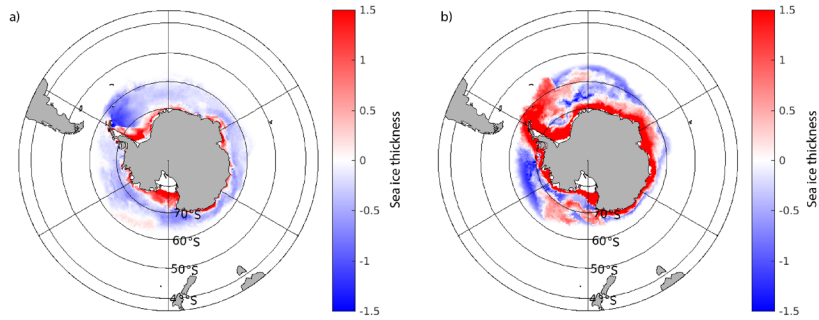


1104

1105 **Figure S8.** Anomaly of net non-solar heat flux at the top of the ocean (in $W m^{-2}$) averaged over the
 1106 ocean region south of $60^{\circ}S$ compared to the corresponding reference simulation in the group of
 1107 experiments starting in March (top row) and September (bottom) for the NEMO (left column) and
 1108 PARASO configurations (right column).

1109

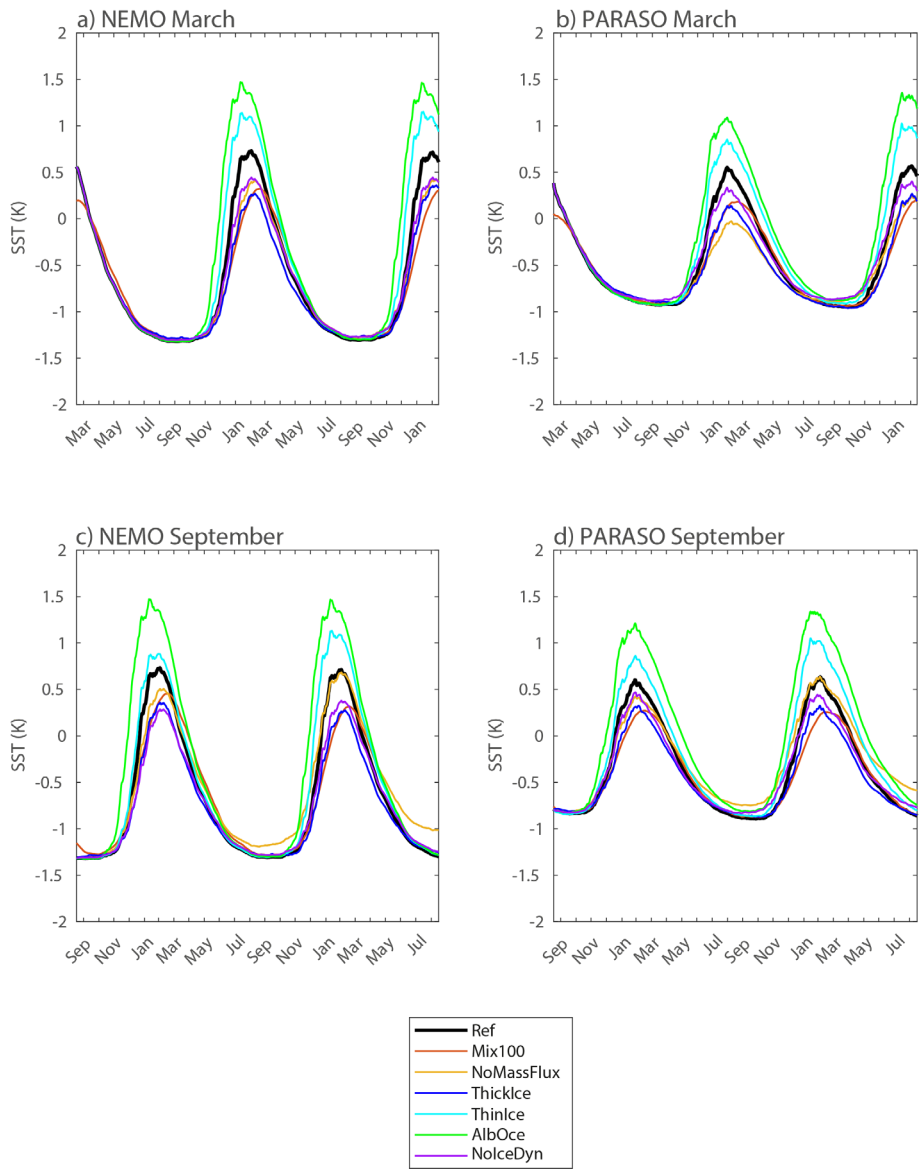
1110



1111

1112 [Figure S9.](#) Difference in sea ice thickness (in m) in September of the second year between
1113 NoIceDYN_NEMO_Mar (left) and NoIceDYN_PARA_Mar (right) and the corresponding reference
1114 experiments.

1115



1116
 1117 **Figure S10.** Sea surface temperature (in K) averaged over the ocean region south of 60°S in the group
 1118 of experiments starting in March (top row) and September (bottom) for the NEMO (left column) and
 1119 PARASO configurations (right column).

1120
 1121
 1122